

Clouds and the Earth's Radiant Energy System (CERES) Energy Balanced and Filled (EBAF) Top-of-Atmosphere (TOA) Edition-4.0 Data Product

NORMAN G. LOEB AND DAVID R. DOELLING

NASA Langley Research Center, Hampton, Virginia

HAILAN WANG

Science Systems and Applications, Inc., Hampton, Virginia

WENYING SU

NASA Langley Research Center, Hampton, Virginia

CATHY NGUYEN, JOSEPH G. CORBETT, LUSHENG LIANG, CRISTIAN MITRESCU, AND FRED G. ROSE

Science Systems and Applications, Inc., Hampton, Virginia

SEIJI KATO

NASA Langley Research Center, Hampton, Virginia

(Manuscript received 30 March 2017, in final form 18 September 2017)

ABSTRACT

The Clouds and the Earth's Radiant Energy System (CERES) Energy Balanced and Filled (EBAF) top-of-atmosphere (TOA), Edition 4.0 (Ed4.0), data product is described. EBAF Ed4.0 is an update to EBAF Ed2.8, incorporating all of the Ed4.0 suite of CERES data product algorithm improvements and consistent input datasets throughout the record. A one-time adjustment to shortwave (SW) and longwave (LW) TOA fluxes is made to ensure that global mean net TOA flux for July 2005–June 2015 is consistent with the in situ value of 0.71 W m^{-2} . While global mean all-sky TOA flux differences between Ed4.0 and Ed2.8 are within 0.5 W m^{-2} , appreciable SW regional differences occur over marine stratocumulus and snow/sea ice regions. Marked regional differences in SW clear-sky TOA flux occur in polar regions and dust areas over ocean. Clear-sky LW TOA fluxes in EBAF Ed4.0 exceed Ed2.8 in regions of persistent high cloud cover. Owing to substantial differences in global mean clear-sky TOA fluxes, the net cloud radiative effect in EBAF Ed4.0 is -18 W m^{-2} compared to -21 W m^{-2} in EBAF Ed2.8. The overall uncertainty in $1^\circ \times 1^\circ$ latitude–longitude regional monthly all-sky TOA flux is estimated to be 3 W m^{-2} [one standard deviation (1σ)] for the *Terra*-only period and 2.5 W m^{-2} for the *Terra–Aqua* period both for SW and LW fluxes. The SW clear-sky regional monthly flux uncertainty is estimated to be 6 W m^{-2} for the *Terra*-only period and 5 W m^{-2} for the *Terra–Aqua* period. The LW clear-sky regional monthly flux uncertainty is 5 W m^{-2} for *Terra* only and 4.5 W m^{-2} for *Terra–Aqua*.

1. Introduction

The top-of-atmosphere (TOA) Earth radiation budget (ERB) represents a balance between incoming solar radiation reaching the TOA and outgoing reflected solar

and thermal radiant energy emitted by the earth-atmosphere system. When the climate system is forced by natural or anthropogenic factors (e.g., changes in solar output, volcanic eruptions, and human activities), an imbalance in the TOA ERB results (Hansen et al. 2011; Loeb et al. 2012; Trenberth et al. 2014; von Schuckmann et al. 2016). Superimposed on this climate change signal is the large internal variability of the climate system, which also causes variations in the ERB. Internal variations can occur over a range of time-space scales, associated with synoptic weather events,

 Denotes content that is immediately available upon publication as open access.

Corresponding author: Dr. Norman G. Loeb, norman.g.loeb@nasa.gov

DOI: 10.1175/JCLI-D-17-0208.1

© 2018 American Meteorological Society. For information regarding reuse of this content and general copyright information, consult the [AMS Copyright Policy \(www.ametsoc.org/PUBSReuseLicenses\)](http://www.ametsoc.org/PUBSReuseLicenses).

TABLE 1. Processing descriptions for CERES level 1–3 data products.

Level	Description	Data product
0	Raw digitized instrument data for all engineering and science data streams in Consultative Committee for Space Data Systems (CCSDS) packet format.	—
1B	Instantaneous filtered broadband radiances at the CERES footprint resolution, geolocation and viewing geometry, solar geometry, satellite position and velocity, and all raw engineering and instrument status data.	Bidirectional scans (BDS)
2	Instantaneous geophysical variables at the CERES footprint resolution. Includes some level-1B parameters and retrieved or computed geophysical variables (e.g., filtered and unfiltered radiances, viewing geometry, radiative fluxes, imager radiances, and cloud and aerosol properties).	SSF
3	Radiative fluxes and cloud properties spatially averaged onto a uniform grid. Includes either instantaneous averages sorted by hour in UTC or temporally interpolated averages at 1-hourly, 3-hourly, daily, monthly, or monthly hourly intervals.	SSF1deg-hour, SSF1deg-day, SSF1deg-month, SYN1deg-1hour, SYN1deg-3hour, SYN1deg-day, SYN1deg-month, or SYN1deg-mhour

atmosphere–ocean interactions [e.g., El Niño–Southern Oscillation (ENSO)], volcanic eruptions, and low-frequency multidecadal fluctuations [e.g., Pacific decadal oscillation (PDO)]. The regional distribution of the net downward radiation at the TOA is coupled to the general circulation of the atmosphere and oceans, which transport surplus energy absorbed in the tropics to polar regions (Trenberth and Caron 2001; Trenberth and Fasullo 2008; Stephens et al. 2015). Because TOA ERB is such a fundamental property of the climate system, ERB observations are widely used for climate model evaluation.

The overarching goals of the Clouds and the Earth's Radiant Energy System (CERES) are to (i) produce a long-term, integrated global climate data record (CDR) for detecting decadal changes in the ERB from the surface to the TOA together with the associated cloud and aerosol properties; (ii) enable improved understanding of the variability in Earth's radiation budget and the role clouds and aerosols play; and (iii) provide data products for climate model evaluation and improvement.

CERES instruments fly on the *Terra*, *Aqua*, *Suomi National Polar-Orbiting Partnership (SNPP)*, and *NOAA-20* satellites. *Terra* is in a descending sun-synchronous orbit with an equator-crossing time of 1030 local time, while *Aqua*, *SNPP*, and *NOAA-20* are in ascending sun-synchronous orbits with a 1330 local time equator-crossing time. Each CERES instrument measures filtered radiances in the shortwave (SW; wavelengths between 0.3 and 5 μm), total (TOT; wavelengths between 0.3 and 200 μm), and window (WN; wavelengths between 8 and 12 μm) regions (CERES on *NOAA-20* replaces the WN channel with a longwave

channel). The filtered radiances are converted to unfiltered SW, longwave (LW), and WN radiances following Loeb et al. (2001), which in turn are converted to instantaneous TOA radiative fluxes using empirical angular distribution models (Su et al. 2015a). A reference level of 20 km is assumed for defining TOA fluxes. This was shown to be the optimal reference level for ERB studies (Loeb et al. 2002). The CERES instruments provide global coverage daily, and monthly mean regional fluxes are based upon daily samples over the entire globe. The standard CERES data products (Table 1) are produced using data from the CERES instrument together with coincident imager data from the Moderate Resolution Imaging Spectrometer (MODIS) and the Visible Infrared Imaging Radiometer Suite (VIIRS). To provide a diurnally complete representation of Earth's radiation budget, all available geostationary imager data between 60°S and 60°N are also used to account for cloud-radiation changes between CERES observation times.

The CERES Energy Balanced and Filled (EBAF) product is produced to address two shortcomings in the standard CERES level-3 data products. First, satellite instruments used to produce CERES TOA ERB data products provide excellent spatial and temporal coverage and therefore are a useful means of tracking variations in ERB over a range of time–space scales. However, the absolute accuracy requirement necessary to quantify Earth's energy imbalance (EEI) is daunting. The EEI is a small residual of TOA flux terms on the order of 340 W m^{-2} . EEI ranges between 0.5 and 1 W m^{-2} (von Schuckmann et al. 2016), roughly 0.15% of the total incoming and outgoing radiation at the

TOA. Given that the absolute uncertainty in solar irradiance alone is 0.13 W m^{-2} (Kopp and Lean 2011), constraining EEI to 50% of its mean ($\sim 0.25 \text{ W m}^{-2}$) requires that the observed total outgoing radiation is known to be 0.2 W m^{-2} , or 0.06%. The actual uncertainty for CERES resulting from calibration alone is 1% SW and 0.75% LW radiation [one standard deviation (1σ)], which corresponds to 2 W m^{-2} , or 0.6% of the total TOA outgoing radiation. In addition, there are uncertainties resulting from radiance-to-flux conversion and time interpolation. With the most recent CERES edition-4 instrument calibration improvements, the net imbalance from the standard CERES data products is approximately 4.3 W m^{-2} , much larger than the expected EEI. This imbalance is problematic in applications that use ERB data for climate model evaluation, estimations of Earth's annual global mean energy budget, and studies that infer meridional heat transports. CERES EBAF addresses this issue by applying an objective constraint algorithm to adjust SW and LW TOA fluxes within their ranges of uncertainty to remove the inconsistency between average global net TOA flux and heat storage in the earth-atmosphere system (Loeb et al. 2009).

Second, the standard CERES level-3 data products (Table 1) provide clear-sky TOA flux maps by averaging all CERES footprints within a region that are completely cloud free as identified by a cloud detection algorithm (Q. Z. Trepte et al. 2017, unpublished manuscript), which uses pixel-level 1-km MODIS measurements as input. However, because of the relatively coarse spatial resolution of the CERES instruments ($\sim 20 \text{ km}$ at nadir), cloud-free conditions at the CERES footprint scale are not always observed, resulting in monthly mean clear-sky TOA flux maps with many missing regions. In EBAF, we address this problem by also inferring TOA fluxes from clear portions of partly cloudy CERES footprints to produce a clear-sky TOA flux climatology free of any missing regions.

EBAF Edition 4.0 (Ed4.0) leverages off of the many algorithm improvements that have been made in the edition-4 suite of CERES level-1–3 data products (Table 1). These include improved instrument calibration, cloud properties, angular distribution models (ADMs) for radiance-to-flux conversion, and use of 1-hourly instead of 3-hourly geostationary (GEO) imager data for time interpolation. CERES Ed4.0 products are based upon consistent meteorological assimilation data (GEOS-5.4.1) throughout, and MODIS radiances and aerosols are from collection 5 (C5) through February 2017 (C6 superseded C5 starting in March 2017). TOA fluxes are constrained using the same approach as EBAF Ed2.8 but using 10 years of Argo (Roemmich

et al. 2009) instead of 5 years. For the first time, EBAF will also provide some basic cloud properties derived from MODIS alongside TOA fluxes. While this paper focuses on TOA radiative fluxes, CERES data products also provide surface ERB at hourly to monthly temporal resolutions (Rutan et al. 2015; Kato et al. 2013). A monthly CERES EBAF-surface Ed4.0 product constrained by TOA fluxes in EBAF-TOA Ed4.0 has been released and is documented in Kato et al. (2017, manuscript submitted to *J. Climate*).

In the following, we provide a detailed description of the methodology used to produce the EBAF Ed4.0 dataset. We present a schematic (see Fig. 1) summarizing the main processing steps involved and describe the key input data products EBAF relies upon (section 2). Methodological differences and direct comparisons between EBAF Ed4.0 and Ed2.8 are discussed in section 3. Finally, we use various methods to estimate the uncertainties in regional mean TOA fluxes (section 4).

2. Data and methods

a. Input data

EBAF Ed4.0 is produced using the Single Scanner Footprint TOA/Surface Fluxes and Clouds (SSF) Ed4A product and slightly modified versions of the algorithms used to produce the CERES SSF 1° (SSF1deg) and synoptic 1° (SYN1deg) Ed4A data products. These data products are the culmination of several processing steps, as summarized in Table 1. To produce the SSF data product, raw digitized instrument data (level 0) are converted to instantaneous filtered radiances (level 1b) using the latest CERES gains (Loeb et al. 2016). Time-dependent spectral response function values are then used to correct for the imperfect spectral response of the instrument and convert the filtered radiances into unfiltered SW, LW, and WN radiances (Loeb et al. 2001, 2016). Since there is no LW channel on CERES, LW daytime radiances are determined from the difference between the TOT and SW channel radiances. Instantaneous TOA radiative fluxes (level 2) are estimated from unfiltered radiances using empirical ADMs (Su et al. 2015a) for different scene types. The SSF product merges CERES footprint parameters including time, position, viewing geometry, radiances, and radiative fluxes with data from the MODIS instrument, which is used to characterize the clear and cloudy portions of a CERES footprint. SSF imager parameters include radiances in many spectral bands averaged over clear, cloudy, and total footprint areas; cloud properties based upon Minnis et al. (2017, manuscript submitted to *IEEE Trans. Geosci. Remote Sens.*) cloud retrieval code; and

aerosol property retrievals from Remer et al. (2008), Levy et al. (2013), and Hsu et al. (2004, 2006). The SSF product also includes meteorological parameters (e.g., surface wind speed, skin temperature, and precipitable water) from the Global Modeling and Assimilation Office (GMAO)'s Goddard Earth Observing System Data Assimilation System (GEOS-DAS V5.4.1) product (Rienecker et al. 2008).

Observed TOA fluxes in the CERES SSF1deg and SYN1deg data products (level 3) are determined by spatially averaging the instantaneous TOA flux values on a 1° equal-area grid (see Table 1 of Doelling et al. 2013), temporally interpolating between observed values at 1-h increments for each hour in coordinated universal time (UTC) of every month, and then averaging all hour boxes in a month (Doelling et al. 2013). The fluxes are then output to a complete 360×180 gridpoint $1^\circ \times 1^\circ$ grid.

The SSF1deg and SYN1deg data products differ primarily by the temporal interpolation methods used. In the SW, the approach for SSF1deg assumes the scene properties between CERES observation times remain invariant. SW radiative fluxes between CERES observation times are determined from the observed fluxes and scene-dependent diurnal albedo models, which describe how TOA albedo (and therefore flux) changes with solar zenith angle for each local time. The sun-angle-dependent diurnal albedo models are based upon the CERES ADMs developed for the Tropical Rainfall Measuring Mission (TRMM) satellite for ocean and land (Loeb et al. 2003) and *Terra* and *Aqua* over snow and sea ice (Su et al. 2015a). The LW fluxes in each hour box between CERES observations are determined by linear interpolation of LW fluxes over ocean, while daytime and nighttime observations over land and desert are interpolated by fitting a one-half sine curve to the observations to account for the much stronger diurnal cycle over land and desert (Young et al. 1998).

In the SYN1deg data product, changes in clouds and radiation between CERES observation times are explicitly accounted for by supplementing CERES observations with 1-hourly imager data from five contiguous GEO satellites covering 60°S – 60°N at any given time. The GEO data are first screened for bad scan lines, and radiances are calibrated against coincident MODIS radiances prior to being used. The GEO imager data are processed using algorithms that closely resemble those used to produce cloud properties and TOA fluxes in the SSF data product. Additional steps are used to convert the GEO imager radiances to broadband TOA fluxes. To remove any GEO-derived flux biases, the fluxes are normalized to CERES at *Terra* or *Aqua* observation times to remain consistent with the CERES instrument

calibration (Doelling et al. 2013). With 1-hourly GEO sampling, GEO SW fluxes are found to be spurious for solar zenith angles greater than 60° as a result of the imperfect GEO cloud properties required for the scene type selection in the narrowband-to-broadband (NB2BB) and ADM models used to convert the GEO radiances into SW fluxes. Therefore, sun-angle-dependent diurnal albedo models are used to estimate the hourly SW fluxes for solar zenith angles greater than 60° in order to compute the daily flux. Detailed descriptions of the steps used to infer broadband TOA fluxes from GEO data and how they are merged with CERES observations are provided in Doelling et al. (2013, 2016). Since the start of the CERES record, a total of 18 GEO imagers of varying quality have been processed to produce the SYN1deg product. With the newest generation of GEO imagers (e.g., *Himawari-8*), the quality of the data has improved markedly.

Clear-sky TOA fluxes in both CERES SSF1deg and SYN1deg are only determined for CERES footprints with cloud fraction $\leq 0.1\%$. Consequently, regions with persistent cloud cover frequently have no clear-sky TOA flux values, even after sampling over a month. Because GEO imager data are less capable than MODIS at screening clouds owing to the smaller number of GEO imager spectral channels, broader spectral channels, and coarser spatial resolution compared to MODIS, GEO imager data are not used to derive clear-sky TOA fluxes in SYN1deg. Instead, the same clear-sky TOA fluxes are used in both SYN1deg and SSF1deg, determined using the temporal interpolation methodology of SSF1deg (described above).

Time-varying instantaneous total solar irradiance (TSI) data are provided in the SSF product and used in level-3 processing to determine spatially and temporally average daily and monthly solar irradiance. The TSIs are obtained from various data sources for the CERES period (Table 2), which are adjusted to a common reference provided by the Solar Radiation and Climate Experiment (SORCE; launched 25 January 2003) Total Irradiance Monitor (TIM) TSI V-15 dataset. The SORCE TIM instrument measures the absolute intensity of solar radiation, integrated over the entire solar disk and the entire solar spectrum reported at the mean solar distance of 1 astronomical unit (ua). TIM is an ambient temperature active cavity radiometer that uses electrical substitution radiometers (ESRs) to measure TSI to an estimated absolute accuracy of 350 ppm (0.035%). Relative changes in solar irradiance are measured to less than 10 ppm yr^{-1} ($0.001\% \text{ yr}^{-1}$), allowing determination of possible long-term variations in the sun's output (Kopp and Lean 2011).

TABLE 2. TSI datasets used in CERES Ed4.0 processing.

Period	TSI source
1 Mar 2000–24 Feb 2003	Prior to SORCE launch, TSI data are extracted from a composite dataset of the World Radiation Center (WRC), Davos, Switzerland. The file used, “composite_d41_62_0906.dat” was downloaded from the ftp site (ftp://ftp.pmodwrc.ch/pub/data/irradiance/composite). An offset was applied to match with SORCE V-15 data using the common reference period between 25 Feb 2003 and 31 Dec 2003.
25 Feb 2003–30 Jun 2013	SORCE TIM V-15 (Kopp and Lean 2011)
1 Jul 2013–31 Oct 2014	A composite dataset available from the Royal Meteorological Institute of Belgium (RMIB) (Mekaoui and Dewitte 2008). It is based on the Differential Absolute Radiometer (DIARAD)/Variability of Solar Irradiance and Gravity Oscillations (VIRGO) dataset (Dewitte et al. 2004) and absolutely calibrated according to Dewitte et al. 2013. This dataset was radiometrically scaled to SORCE TIM V-15 using an offset, determined over a common 5-yr period (1 Mar 2003–29 Feb 2008).
1 Nov 2014–present	SORCE TIM V-17 with offset applied to bring V-17 in line with V-15.

Daily and monthly regional average incident solar fluxes are determined by first analytically solving the integral of the cosine of the solar zenith angle μ_o within a hour box defined in coordinated universal time for all hour boxes during the month. The integrated μ_o for the hour box is then multiplied by TSI corrected for Earth–sun distance to obtain the hour-box average TSI. The solar ephemeris (solar declination angle, Earth–sun distance factor, and equation of time) is updated hourly. The daily incident solar flux is the average of the 24-hourly TSIs contained in the day. Similarly, the monthly incident solar flux is the average of the daily TSIs within the month. To provide a more accurate representation of TSI within a 1° grid box, rather than compute it only once at the midpoint, we compute the solar incoming

twice at latitudes $\pm 0.25^\circ$ from the midpoint and then average the results.

To determine global mean quantities in edition 4, Earth is assumed to be an oblate spheroid instead of a sphere. Thus, when the annual cycle in Earth’s declination angle and Earth–sun distance are accounted for, the well-known $S_o/4$ expression for the mean solar irradiance of a spherical Earth becomes $S_o/4.003$ for an oblate spheroid, where S_o is the TSI.

b. EBAF Ed4.0 TOA flux determination

1) ALL SKY

Figure 1 provides a schematic of the processing steps involved in producing CERES EBAF Ed4.0 TOA

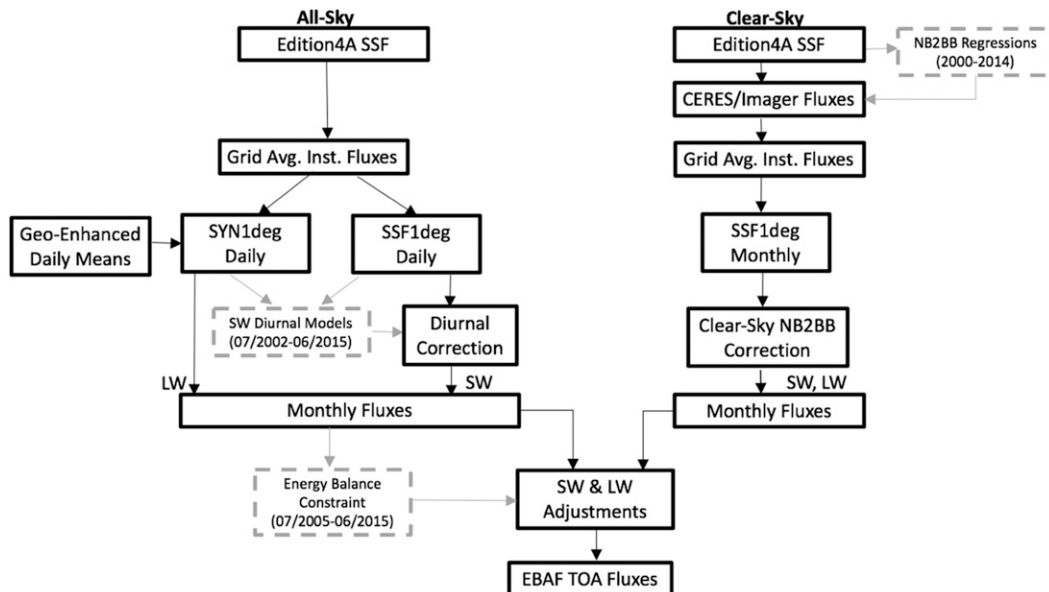


FIG. 1. Processing flow for EBAF-TOA. Gray boxes and arrows correspond to processes that are performed only once prior to production (“preprocessing” steps). Black boxes and arrows are processing steps performed routinely.

fluxes. Instantaneous all-sky TOA fluxes from the SSF edition-4A product are first averaged regionally onto a $1^\circ \times 1^\circ$ equal-area grid and sorted by hour in coordinated universal time. Time interpolation is then applied to produce SYN1deg and SSF1deg daily mean fluxes. Because the GEO imager infrared bands are generally stable owing to the availability of onboard blackbody sources for calibration, LW monthly mean TOA fluxes are computed directly from SYN1deg daily mean LW TOA fluxes. In the SW, the situation is more complicated. While the SYN1deg approach provides improved diurnal coverage by merging CERES and 1-hourly GEO data, artifacts in the GEO imager visible bands over certain regions and time periods can introduce larger regional uncertainties. Spurious jumps in the SW TOA flux record can occur when GEO satellites are replaced, because of changes in satellite position, calibration, visible sensor spectral response, cloud retrieval quality, and imaging schedules. Such artifacts in the GEO data can be problematic in studies of TOA radiation interannual variability and/or trends. In contrast, the SSF1deg product provides global coverage daily with excellent calibration stability but only samples at specific times of the day because of the sun-synchronous orbit. Figure 2 illustrates how GEO artifacts can impact regional trends in SW TOA flux. The trends derived directly from CERES SSF1deg-*Terra-Aqua* are shown in Fig. 2a for July 2002–September 2016, while Fig. 2b shows the difference between SYN1deg-*Terra-Aqua* and SSF1deg-*Terra-Aqua*. The differences in Fig. 2b reach $\pm 2 \text{ W m}^{-2} \text{ decade}^{-1}$ and depend strongly upon GEO domain (indicated by vertical black lines).

To maintain the excellent CERES instrument calibration stability of SSF1deg and also preserve the diurnal information found in SYN1deg, EBAF Ed4.0 uses a new approach that applies predetermined empirical diurnal correction ratios (DCRs) to daily regional mean SSF1deg SW fluxes. These are then averaged to produce monthly SW TOA fluxes that are diurnally complete and analogous to SYN1deg, but without GEO artifacts. The DCRs consist of SYN1deg–SSF1deg flux ratios derived using daily mean SW TOA fluxes between July 2002 and June 2015. The DCRs are defined according to calendar month, surface type, latitude, and a daily diurnal asymmetry ratio (DAR), defined as follows:

$$\text{DAR} = \frac{F^{\text{SW}}(\text{morn}) - F^{\text{SW}}(\text{aft})}{F^{\text{SW}}(24 \text{ h})}, \quad (1)$$

where $F^{\text{SW}}(\text{morn})$ is the mean SW flux corresponding to 0000–1200 local time, $F^{\text{SW}}(\text{aft})$ is the mean SW flux corresponding to 1200–2400 local time, and $F^{\text{SW}}(24 \text{ h})$ is the mean 24-h SW flux. DAR is derived using GEO

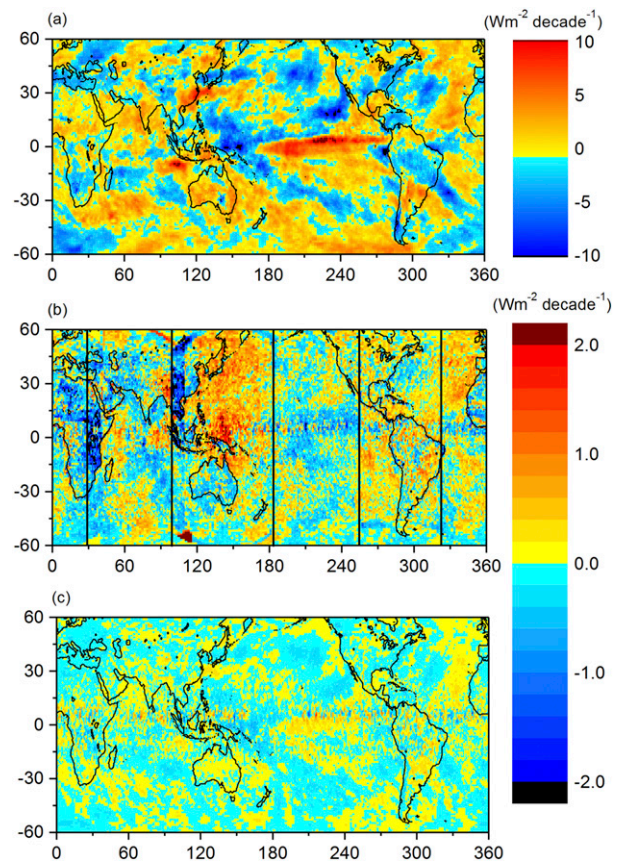


FIG. 2. (a) Trend in SW TOA flux anomalies from SSF1deg-*Terra-Aqua* for July 2002–September 2016. Trend difference relative to SSF1deg-*Terra-Aqua* for (b) SYN1deg-*Terra-Aqua* and (c) EBAF Ed4.0. Vertical lines in (b) correspond to GEO boundaries.

imager data only and provides a measure of SW TOA flux difference associated with cloud changes between morning and afternoon. Because DAR is a difference between morning and afternoon TOA SW fluxes and is normalized by the 24-h flux, the impact of any systematic GEO imager calibration errors is minimized. In addition, because a single set of DCRs are applied to SSF1deg SW fluxes over the entire CERES record, the stability of the record is more closely tied to that of the CERES instruments than SYN1deg.

Figure 3 provides an example of the regional monthly mean DAR for October 2008. In the stratocumulus regions off the west coasts of North and South America and Africa, DAR is strongly positive since cloud fraction in these regions reaches a maximum in early morning and decreases in the afternoon due mainly to the diurnal cycle of solar insolation and absorption of solar radiation in the upper regions of the cloud (Wood 2012). Over land, DAR tends to be negative because convection is generally stronger in the afternoon.

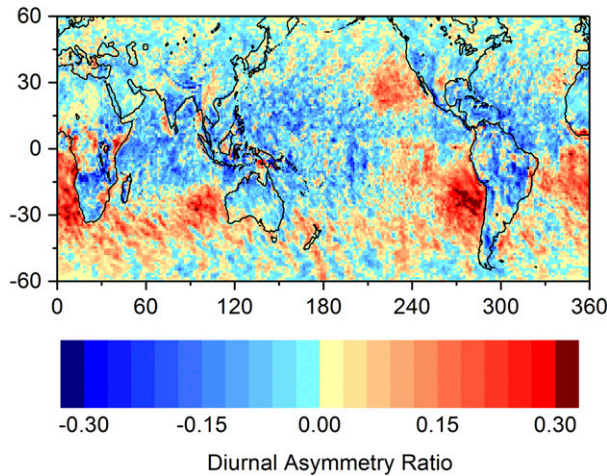


FIG. 3. Monthly regional mean DAR for October 2008.

For each calendar month between July 2002 and June 2015, DCRs are derived from daily SSF1deg and SYN1deg TOA SW fluxes defined for ocean, land, and desert surfaces for DAR increments of 0.05 (for snow and sea ice no correction is applied). The DCRs are derived using a 15° latitude running average at 1° latitude increments between 60°S and 60°N . We only consider the combined *Terra–Aqua* SYN1deg product to determine the numerator in the SYN1deg–SSF1deg ratio as this is the most diurnally complete version available. The denominator is determined from either SSF1deg–*Terra* or SSF1deg–*Terra–Aqua*. DCRs generated using only SSF1deg–*Terra* in the denominator are applied during the *Terra*-only period (March 2000–June 2002), while a combined *Terra–Aqua* DCR is used for July 2002 onward. In the event that *Terra* or *Aqua* data are missing during the latter period, DCR corrections based upon *Aqua* only or *Terra* only are used.

Figure 4 shows an example of DCRs for ocean centered at 29.5°S in July for *Terra* only and for *Terra* and *Aqua* combined. Because *Terra* is a morning satellite, the *Terra*-based DCR is smaller (greater) than 1 when DAR is positive (negative). The correction reaches 20% at DAR values of ± 0.6 . In contrast, DCRs when *Terra* and *Aqua* are combined are much closer to 1. Thus, the SSF1deg SW flux requires a much smaller diurnal correction when both *Terra* and *Aqua* are combined compared to the *Terra*-only case.

To assess the performance of this approach, we compare SSF1deg-based TOA fluxes with those from SYN1deg–*Terra–Aqua* before and after applying the DCRs for October 2008 (Figs. 5a–d). With no diurnal corrections made to *Terra*-only SSF1deg, monthly mean temporal interpolation errors reach close to 30 W m^{-2} off the coast of South America

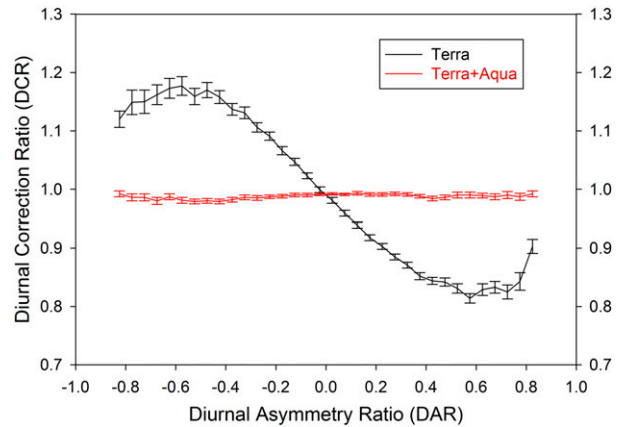


FIG. 4. DCRs for latitude centered over 29.5°S over ocean in July. Error bars correspond to standard error in DCR.

over marine stratocumulus and -20 W m^{-2} over the land convection regions of South America and southern Africa (Fig. 5a). After applying DCRs to SSF1deg–*Terra*, the differences are significantly reduced (Fig. 5c). The root-mean-square (RMS) error between 60°S and 60°N is reduced from 4.5 to 2.7 W m^{-2} after applying the DCRs. For the *Terra–Aqua* period, there is a dramatic improvement in the uncorrected SSF1deg result (Fig. 5b) compared to the *Terra*-only case (Fig. 5a). The regional RMS error for SSF1deg–*Terra–Aqua* is 2.2 W m^{-2} and further decreases to 1.9 W m^{-2} after applying DCRs (Fig. 5d). Table 3 compares the mean bias and standard deviation in SW TOA flux monthly averages over 60°S – 60°N for all months between July 2002 and June 2015 before and after diurnal corrections are applied to SSF1deg–*Terra*, SSF1deg–*Aqua*, and SSF1deg–*Terra–Aqua* daily means. After applying the diurnal corrections, the mean bias of a few tenths of a watt per meter squared is removed and the standard deviation in the bias is reduced by a factor of approximately 4 for *Terra* only and *Aqua* only and by 55% for *Terra* and *Aqua* combined.

After applying the DCRs to daily mean SSF1deg SW TOA fluxes, monthly averages are then calculated (Fig. 1). To account for the SW TOA flux contribution for solar zenith angles exceeding 90° , a twilight flux correction is added to the outgoing SW flux in order to take into account the atmospheric refraction of light. The magnitude of this correction varies with latitude and season and is determined only for all-sky conditions using the observed climatological mean values of Kato and Loeb (2003). In general, the regional correction is less than 0.5 W m^{-2} and the global mean correction is 0.2 W m^{-2} . Because of the contribution of twilight, there are regions near the terminator in which outgoing SW TOA flux can exceed the incoming solar radiation. In

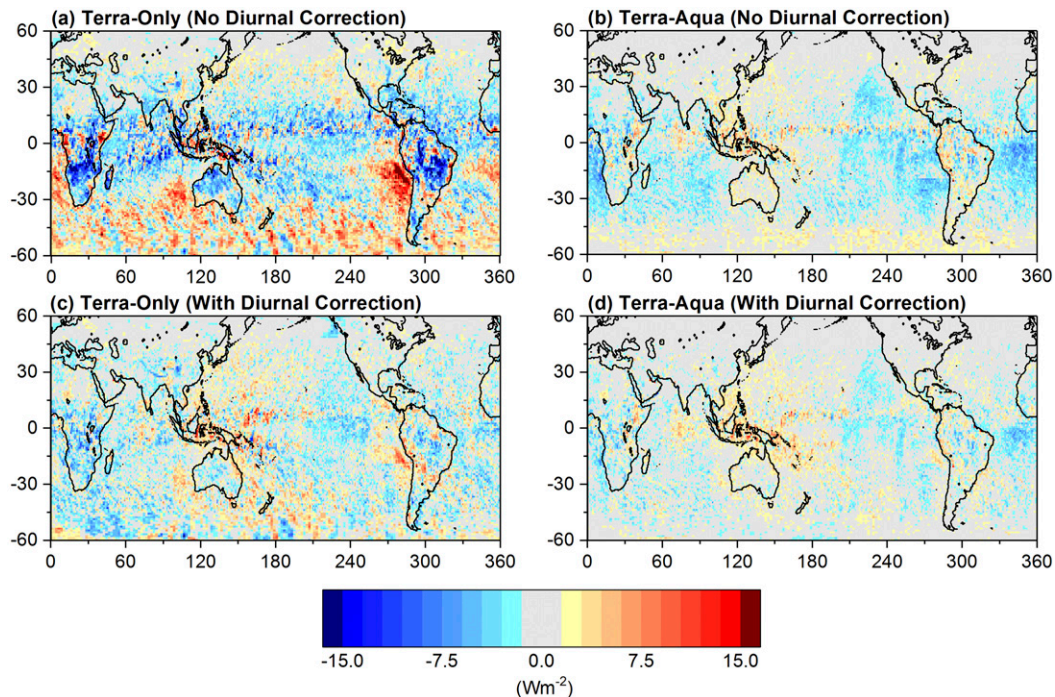


FIG. 5. All-sky SW TOA flux difference relative to SYN1deg-*Terra-Aqua* for October 2008 with no diurnal correction to SSF1deg for (a) *Terra* only and (b) *Terra-Aqua* and after applying DCRs to SSF1deg for (c) *Terra* only and (d) *Terra-Aqua*.

these cases, the albedo (defined as the ratio of outgoing SW to incoming solar radiation) can exceed unity. The final step is to apply the SW and LW TOA flux energy balance adjustments, described in section 2b(3).

As noted earlier, the use of DCRs preserves the stability of the CERES record without introducing GEO artifacts like those in Fig. 2b. This is illustrated in Fig. 2c, which compares trends in SW TOA flux anomalies from the final EBAF Ed4.0 product with those from SSF1deg.

2) CLEAR SKY

The processing steps used to produce EBAF clear-sky TOA fluxes are also illustrated in Fig. 1. To increase

sampling, CERES-derived clear-sky TOA fluxes in SSF Edition 4A are supplemented by TOA fluxes inferred from MODIS radiances. For each day and region, a grid-box average clear-sky TOA flux is determined from an area-weighted average of instantaneous CERES broadband fluxes for completely cloud-free CERES footprints and MODIS-derived “broadband” clear-sky fluxes estimated from the cloud-free portions of CERES footprints. A clear-sky CERES footprint is defined as having a cloud fraction $\leq 0.1\%$. MODIS-derived clear-sky fluxes are inferred for CERES footprints with cloud fraction $> 0.1\%$ and $< 95\%$. Clear regions within CERES footprints are identified using the CERES cloud mask applied to MODIS 1-km pixel data, which is based upon Q. Z. Trepte et al. (2017, unpublished manuscript). Clear-sky fluxes in partly cloudy CERES footprints are derived using MODIS-CERES narrowband-to-broadband regressions to convert MODIS narrowband radiances averaged over the clear portions of a footprint to broadband radiances. The narrowband-to-broadband regressions are developed from cloud-free CERES footprints from every second year between 2002 and 2014 for *Aqua* and between 2000 and 2005 for *Terra*. Separate regressions are derived for each calendar month by combining all Januaries, Februaries, etc., of all years over these periods. Table 4 lists the MODIS spectral channels used in the

TABLE 3. Mean bias and standard deviation in SW TOA flux (W m^{-2}) monthly averages for 60°S – 60°N relative to SYN1deg-*Terra-Aqua* for July 2002–June 2015 before and after diurnal corrections are applied to SSF1deg-*Terra*, SSF1deg-*Aqua*, and SSF1deg combined *Terra* and *Aqua* daily means.

	Before diurnal correction		After diurnal correction	
	Mean bias	Std dev	Mean bias	Std dev
<i>Terra</i> -only	−0.19	0.38	−0.04	0.08
<i>Aqua</i> -only	−0.32	0.51	0.09	0.13
<i>Terra</i> and <i>Aqua</i>	−0.30	0.13	0.05	0.08

TABLE 4. Specific information about the narrowband-to-broadband regressions used to infer broadband radiances from MODIS narrowband channels.

Shortwave narrowband-to-broadband regressions	
MODIS spectral channels (μm)	0.47, 0.65, 0.86, and 1.63 (<i>Terra</i>) or 2.13 (<i>Aqua</i>)
Surface types	Ocean, forests, savannas, grassland/crops, dark desert, bright desert, fresh snow, sea ice, and permanent snow (Greenland and Antarctica).
Viewing zenith angle	Seven bins from 0° to 70° in 10° increments.
Solar zenith angle	Nine bins from 0° to 90° in 10° increments.
Relative azimuth angle	Nine bins from 0° to 180° in 20° increments.
Longwave narrowband-to-broadband regressions (separate for daytime and nighttime)	
MODIS spectral channels (μm)	6.7, 8.5, 11.0, 12.1, and 14.2
Surface types	Same as for SW (above).
Viewing zenith angle	Same as for SW (above).
Precipitable water (cm)	0.0–1.0, 1.0–3.0, 3.0–5.0, and 5.0–10.0 (snow/sea ice free) 0.0–0.2, 0.2–0.4, 0.4–0.6, and 0.6–10 (snow/sea ice)

narrowband-to-broadband regressions and shows how the regressions are stratified according to surface type, viewing geometry, and precipitable water (LW only). To reduce the likelihood of including CERES footprints containing misclassified clear areas due to undetected cloud contamination, the narrowband-to-broadband regressions are only applied if the clear area imager $0.65\text{-}\mu\text{m}$ reflectance standard deviation <0.037 and the $11\text{-}\mu\text{m}$ radiance standard deviation $<0.124\text{ W m}^{-2}\text{ sr}^{-1}\mu\text{m}^{-1}$. These thresholds are derived using the 99th percentiles of footprints with a clear fraction $>99.9\%$. Relative to all nonovercast CERES footprints, only 0.5% of CERES footprints are rejected based upon these criteria. The “broadband” MODIS radiances are then converted to TOA radiative fluxes using CERES clear-sky ADMs.

Daily mean clear-sky SW and LW TOA fluxes are determined using the SSF1deg time interpolation methodology. In the SW, monthly mean clear-sky fluxes are obtained by weighting the daily mean SW fluxes by the gridbox clear area fraction. The clear area fraction weighting is applied in order to reduce the influence of cloud contamination, which can occur as a result of subpixel-scale clouds (e.g., trade cumulus) and/or enhanced scattering from adjacent clouds into the clear regions. Indeed, we find that daily mean clear-sky SW TOA fluxes show a linear increase with gridbox cloud fraction that exceeds theoretical values accounting for increases in aerosol humidification near clouds, implying that there likely are some misidentified clear areas on days when cloud amount is appreciable. Weighting the daily mean SW clear-sky fluxes by the gridbox clear area fraction reduces the influence of days with possible cloud contamination on the monthly mean. In contrast, daily mean clear-sky LW TOA fluxes are weighted

equally when computing gridbox monthly mean values. We find that clear-sky LW TOA fluxes show little correlation to cloud fraction. Furthermore, offline Fu–Liou radiative transfer model calculations of LW TOA flux initialized using temperature and humidity profiles from GEOS-5 reproduce the spread in observed daily mean values during the course of a month. We suspect that for SW flux, subpixel low clouds are the main reason for the correlation between clear-sky flux and cloud fraction. In the LW, contamination by low-level clouds is less critical than that from high clouds, which tend to be more extensive and thus more likely to be resolved at the MODIS pixel scale. In addition, weighting of LW flux by clear fraction would mask the effects of upper-tropospheric humidity (UTH) variability on clear-sky LW flux.

In both SW and LW, a correction to narrowband-to-broadband bias errors is made monthly based upon the difference between broadband radiances for cloud-free CERES footprints and the MODIS-based broadband estimate. This ensures that the final product’s calibration is tied to CERES.

Clear-sky TOA fluxes are derived from *Terra* prior to July 2002 (the first month of CERES *Aqua* data) and *Aqua* thereafter. MODIS–*Aqua* is preferred over MODIS–*Terra* after July 2002 because it is more stable radiometrically throughout the *Aqua* period, especially for the water vapor channel (Sun et al. 2014). To avoid a clear-sky TOA flux discontinuity between the *Terra*-only (March 2000–June 2002) and *Aqua* periods (July 2002 onward), an adjustment is applied to clear-sky fluxes during the *Terra*-only period. The adjustment is derived using data from 2003–07. For each calendar month, we compute the regional climatology of the *Aqua*–*Terra* difference and use that difference to adjust

TABLE 5. Global mean TOA fluxes (W m^{-2}) for July 2005–June 2015 before and after applying net TOA flux constraint for EBAF Ed2.8 and EBAF Ed4.0.

	EBAF Ed2.8		EBAF Ed4.0	
	Unadjusted	With constraint	Unadjusted	With constraint
Incoming Solar	339.8	339.8	340.0	340.0
All-sky LW	238.7	239.6	238.6	240.1
All-sky SW	97.9	99.6	97.1	99.1
All-sky net	3.2	0.63	4.3	0.71
Clear-sky LW	264.5	265.4	266.3	268.1
Clear-sky SW	51.5	52.5	52.3	53.3
Clear-sky net	23.8	21.9	21.4	18.6
LW CRE	25.8	25.8	27.7	27.9
SW CRE	−46.4	−47.1	−44.8	−45.8
Net CRE	−20.6	−21.3	−17.1	−17.9

Terra clear-sky fluxes during the *Terra*-only period. The adjustment removes first-order *Terra*–*Aqua* differences, thereby avoiding a discontinuity due to inconsistencies between *Terra* and *Aqua* clear-sky algorithms (cloud mask, ADMs, etc.).

It should be noted that while EBAF clear-sky TOA fluxes are representative of cloud-free areas, most climate models compute clear-sky fluxes in both clear and cloudy regions assuming there are no clouds present in the grid box. Because relative humidity in cloud columns is generally greater than in adjacent clear areas, this can lead to a “wet bias” in the models and cause a lower clear-sky LW TOA flux compared to observations. As an example, Fig. 4 of Kato et al. (2013) compares clear-sky TOA flux calculations for clear and cloudy columns assuming no clouds are present (i.e., by “removing” clouds from cloudy columns) with fluxes weighted by the clear area fraction, analogous to what is done in observations. In the LW, differences are larger in regions with persistent high cloud, such as over the South Pacific and South Atlantic convergence zones and over the western tropical Pacific. Biases reach -6 W m^{-2} in those regions. Sohn et al. (2006) note that the LW bias can reach -10 W m^{-2} . At the global scale, the mean difference is -1.25 W m^{-2} in the LW and 0.24 W m^{-2} in the SW (Table 2 in Kato et al. 2013).

3) TOA FLUX ADJUSTMENTS

Despite recent improvements in satellite instrument calibration and the algorithms used to determine CERES TOA radiative fluxes, a sizable imbalance persists in the average global net radiation at the TOA from CERES satellite observations. With no adjustments to CERES SW and LW all-sky TOA fluxes, the net imbalance for July 2005–June 2015 is approximately 4.3 W m^{-2} , much larger than expected. As in previous

versions of EBAF, we use the objective constraint algorithm described in Loeb et al. (2009) to adjust SW and LW TOA fluxes within their ranges of uncertainty to remove the inconsistency between average global net TOA flux and heat storage in the earth–atmosphere system, as determined primarily from ocean heat content anomaly (OHCA) data. In the current version, the global annual mean values are adjusted such that the July 2005–June 2015 mean net TOA flux is $0.71 \pm 0.10 \text{ W m}^{-2}$, as provided in Johnson et al. (2016) [uncertainties at the 95% confidence level account for expendable bathythermographs (XBT) correction uncertainties and Argo sampling errors for 0–1800 m]. The uptake of heat by Earth for this period is estimated from the sum of (i) $0.61 \pm 0.09 \text{ W m}^{-2}$ from the slope of weighted linear least squares fit to Argo OHCA data to a depth of 1800 m analyzed following Lyman and Johnson (2008), (ii) $0.07 \pm 0.04 \text{ W m}^{-2}$ from ocean heat storage at depths below 2000 m using data from 1981–2010 (Purkey and Johnson 2010), and (iii) $0.03 \pm 0.01 \text{ W m}^{-2}$ from ice warming and melt and atmospheric and lithospheric warming for 1971–2010 (Rhein et al. 2013). We note that the 0.1 W m^{-2} uncertainty in EEI in Johnson et al. (2016) is at the low end of the uncertainty range compared to other estimates, which typically range between 0.2 and 0.4 W m^{-2} (Abraham et al. 2013; von Schuckmann et al. 2016).

Importantly, the SW and LW TOA flux adjustment is a one-time adjustment to the entire record. Therefore, the time dependence of EBAF TOA flux is tied to the CERES instrument radiometric stability. Table 5 shows how the TOA fluxes change before and after the adjustments are applied for July 2005–June 2015. For comparison, we also provide the corresponding values for EBAF Ed2.8. In the SW, the adjustment process increases TOA flux by 2 W m^{-2} , whereas LW TOA flux increases by 1.5 W m^{-2} . The corresponding adjustments

for EBAF Ed2.8 were 1.5 W m^{-2} for SW and 0.9 W m^{-2} for LW. For consistency, adjustments to the clear-sky TOA fluxes use the same scaling factor as all sky.

4) CLOUD PROPERTIES

For the first time, EBAF-TOA Ed4.0 provides MODIS-based monthly mean cloud properties alongside TOA fluxes. The cloud properties include cloud amount, optical depth, effective pressure, and temperature derived from instantaneous cloud retrievals averaged over CERES footprints provided in the CERES SSF Ed4.0 product. The instantaneous cloud properties in SSF Ed4.0 are based upon Minnis et al. (2017, manuscript submitted to *IEEE Trans. Geosci. Remote Sens.*). In EBAF Ed4.0, the cloud optical depths are based upon daytime MODIS retrievals only, while the remaining cloud properties are computed using both daytime and nighttime data. The monthly mean cloud properties between March 2000 and June 2002 are retrieved from *Terra*-MODIS, while cloud properties from July 2002 onward are determined from the average of *Terra*-MODIS and *Aqua*-MODIS. Because the *Terra*-MODIS cloud properties represent the cloud conditions observed during the *Terra* sun-synchronous orbit overpass time of 1030 local equator-crossing time, they may differ substantially over maritime stratus and land afternoon convection compared to those during the *Terra*-*Aqua* period. As a result, some of the cloud properties may exhibit a discontinuity in some regions in July 2002.

To determine monthly mean cloud properties, we follow the same steps as in the CERES SSF1deg data product (Doelling et al. 2013) but use cloud properties from both *Terra* and *Aqua* to determine the monthly average (SSF1deg cloud properties are produced separately for *Terra* and *Aqua*). The instantaneous cloud properties in the SSF product are spatially averaged into 1° regions. These are then linearly interpolated hourly to estimate cloud conditions between the MODIS-observed measurements. The hourly regional cloud properties, whether observed or interpolated, are then averaged over the month. While cloud fraction is simply averaged, the remaining cloud properties are weighted by cloud fraction. Cloud optical depth is averaged in log form, since log cloud optical depth is approximately proportional to visible radiance. The monthly regional cloud properties within a 1° latitude zone are averaged to compute the zonal mean. The global mean cloud properties are averaged from the zonal means using geodetic weighting.

Because the *Aqua*-MODIS $1.6\text{-}\mu\text{m}$ channel failed shortly after launch, the $1.24\text{-}\mu\text{m}$ channel is used as an alternative in both *Aqua* and *Terra* Ed4.0 daytime cloud optical depth retrievals over snow. However, the

$1.24\text{-}\mu\text{m}$ channel is not optimal for cloud optical depth since surface reflectance can affect retrievals more than the $1.6\text{-}\mu\text{m}$ channel. Surface shortwave downward flux validation of radiative transfer results over dome C using 1.6- and $1.24\text{-}\mu\text{m}$ cloud retrievals anecdotally suggest that the $1.24\text{-}\mu\text{m}$ cloud optical depths for thin clouds over snow can be overestimated by a factor of 2 or more.

Improvements to the CERES cloud algorithm in Ed4.0 compared to earlier versions include using regional mean boundary apparent lapse rates developed using collocated *CALIPSO* and MODIS data to determine low cloud-top height (Sun-Mack et al. 2014), a CO_2 -slicing method to retrieve high cloud over low-lying clouds (Chang et al. 2010), and a rough ice crystal model (Yang et al. 2008) to improve ice cloud retrieval. Minnis et al. (2017, manuscript submitted to *IEEE Trans. Geosci. Remote Sens.*) provide a detailed description of the edition-4 cloud algorithm.

3. Comparisons between EBAF Ed4.0 and EBAF Ed2.8

a. Input data and methodological differences

While the input datasets and methodology used to produce EBAF Ed4.0 are similar to EBAF Ed2.8, a number of important differences are worth highlighting. EBAF Ed2.8 was based upon essentially a hybrid of versions of CERES algorithms and ancillary input datasets. CERES TOA fluxes were based upon Ed3 calibration coefficients, but the MODIS cloud property retrievals and ADMs used in generating the CERES SSF product were based upon Ed2 algorithms, developed early in the CERES project. The meteorological assimilation data used in the cloud algorithm consisted of GEOS-4 for March 2000–December 2007 and GEOS-5.2.1 for January 2008 onward, while MODIS radiance calibration was from collection 4 for March 2000–April 2006 and collection 5 for May 2006 onward. Although these input changes have a small impact on all-sky TOA fluxes in EBAF Ed2.8, they do cause discontinuities in clear-sky TOA fluxes (through scene identification). As in Ed4.0, EBAF Ed2.8 applied SW diurnal corrections to SSF1deg SW TOA fluxes, but relied on a much simpler approach [see Loeb et al. (2012) supplementary information for details].

EBAF Ed4.0 incorporates all of the algorithm improvements that have recently been implemented in creating the Ed4.0 suite of CERES data products. This includes improved instrument calibration, cloud properties, ADMs, and time interpolation and space averaging with hourly GEO imager measurements. In

addition, the meteorological assimilation data used in all Ed4.0 data products are based upon GEOS-5.4.1 throughout the record and MODIS radiances, and aerosol input files are from collection 5 through February 2017. Collection 5 production stopped at the end of February 2017 and was superseded by collection 6.

EBAF Ed4.0 time averaging is performed using coordinated universal time whereas EBAF Ed2.8 used local time. This has implications for regional solar incoming flux. In Ed2.8, the call to solar ephemeris was once per day at 1200 UTC for all regions, whereas for Ed 4.0 we update hourly for each region. As noted earlier, the EBAF Ed4.0 global net TOA flux constraint uses 10 years of Argo instead of 5 years.

Substantial algorithm improvements were made in EBAF Ed4.0 clear-sky flux determination. The greatest improvement is associated with the edition-4 MODIS cloud mask (Minnis et al. 2017, manuscript submitted to *IEEE Trans. Geosci. Remote Sens.*; Q. Z. Trepte et al. 2017, unpublished manuscript). The new cloud mask substantially improves detection of thin cirrus and low cloud, provides a better discrimination between cloud and dust, and substantially improves cloud detection in polar regions. The cloud mask improvements include the use of additional MODIS channels and threshold tests [MODIS 1.38- μm threshold test, $T_{3.7} - T_{11}$ and $T_{11} - T_{12}$ difference tests, 2.1–0.65- μm ratio test, 1.24–0.65- μm ratio test, and new visible (VIS) threshold tests] derived with the benefit of years of *CALIPSO* data for guidance. In contrast, the EBAF Ed2.8 cloud mask was developed prior to *CALIPSO*. As noted earlier, the EBAF Ed4.0 narrowband-to-broadband regressions now use many spectral channels. In EBAF Ed2.8, the narrowband-to-broadband regression was based upon 0.65, 0.86, and 1.63 μm for SW and only one channel (11 μm) for LW. As a result, the magnitude of the required corrections for narrowband-to-broadband error are much smaller in EBAF Ed4.0. In addition, the ADMs used in EBAF Ed4.0 are improved compared to Ed2.8, particularly over ocean and areas affected by heavy aerosol (smoke, dust, and pollution) (Su et al. 2015a). In polar regions, EBAF Ed2.8 only estimates a high-resolution clear-sky flux if the CERES footprint is partly cloudy and has 100% sea ice, 100% open water, or 100% land coverage. This conservative approach excludes footprints with partial sea ice coverage and inadvertently causes clear-sky SW TOA flux to be underestimated over summertime Arctic Ocean. This problem is overcome in EBAF Ed4.0, which estimates high-resolution clear-sky flux if CERES footprint is partly cloudy and partly sea ice/water or partly snow/land. We apply both sets of regressions to clear-sky radiances and weight by surface type coverage. This

increases the clear-sky SW TOA flux over the Arctic Ocean compared to Ed2.8. EBAF Ed4.0 also corrects a coding error found in EBAF Ed2.8 clear-sky time-space averaging involving erroneous use of all-sky instead of clear-sky diurnal albedo models (diurnal models of albedo dependence upon solar zenith angle) for converting instantaneous SW TOA clear-sky fluxes into 24-h averages. This correction increases the magnitude of clear-sky SW TOA flux.

b. Global means

Compared to EBAF Ed2.8, global annual mean all-sky TOA fluxes for EBAF Ed4.0 decrease by 0.5 W m^{-2} in the SW and increase by 0.5 W m^{-2} in the LW (Table 5). In contrast, much larger differences occur for clear-sky TOA fluxes, with EBAF Ed4.0 increasing by 0.8 W m^{-2} in the SW and 2.7 W m^{-2} in the LW relative to EBAF Ed2.8. The main reason for the increase in LW clear-sky TOA flux is due to cloud mask changes between Ed4.0 and Ed2.8. With a more stringent cloud mask, one might also expect the EBAF Ed4.0 global mean SW clear-sky flux to fall below EBAF Ed2.8. However, improvements in dust detection resulted in more dust in EBAF Ed4.0 SW clear-sky flux, which offset the impact of cloud mask changes elsewhere. In addition, correcting the coding error found in EBAF Ed2.8 clear-sky SW TOA flux time-space averaging (section 3a) causes clear-sky SW TOA flux to increase, which further offsets decreases because of cloud mask improvements.

Because of the large changes in clear-sky TOA fluxes, cloud radiative effect (CRE) shows marked differences between EBAF Ed4.0 and Ed2.8 (Table 5). In the LW, CRE increases by 2.2 W m^{-2} , while the magnitude of SW CRE cooling decreases by 1.3 W m^{-2} . Consequently, net CRE changes from -21 W m^{-2} in Ed2.8 to -18 W m^{-2} in Ed4.0. By comparison, Raschke et al. (2016) show that global mean net CRE is -19 W m^{-2} from the Global Energy and Water Exchanges (GEWEX) surface radiation budget (SRB) product and -25 W m^{-2} from the International Satellite Cloud Climatology Project (ISCCP).

c. Regional mean differences

Regional mean all-sky SW and LW TOA flux differences between EBAF Ed4.0 and Ed2.8 are shown in Figs. 6a–d for January and July 2010. For all-sky SW (Figs. 6a,b), EBAF Ed4.0 values exceed Ed2.8 by up to 14 W m^{-2} in January over marine stratocumulus regions, corresponding to about 7.5% relative to the mean. The difference is due to improvements in the diurnal correction in EBAF Ed4.0 that takes advantage of increased sampling of the diurnal cycle with 1-hourly instead of 3-hourly GEO imager data in Ed4.0.

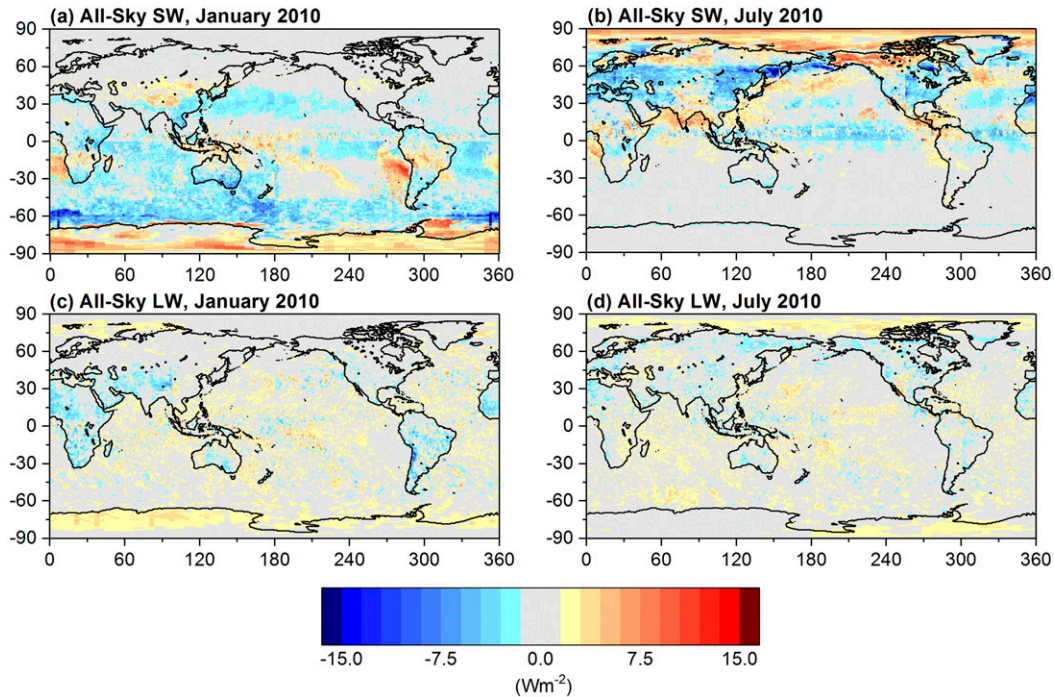


FIG. 6. EBAF Ed4.0 minus Ed2.8 all-sky TOA flux difference in (left) January and (right) July 2010 for (a),(b) SW and (c),(d) LW fluxes.

Differences are also positive in polar regions, reaching 10 W m^{-2} , which are mainly associated with the influence of cloud property differences on instantaneous TOA fluxes in level-2 processing (Su et al. 2015a). The global average regional RMS difference between EBAF Ed4.0 and Ed2.8 SW TOA flux is 2.5 W m^{-2} (Table 6). In the LW (Figs. 6c,d), EBAF Ed4.0 regional all-sky values are generally within 2 W m^{-2} of EBAF Ed2.8, and the global average regional RMS difference is approximately 1.5 W m^{-2} . For net TOA flux, the regional RMS difference is just under 3 W m^{-2} .

For clear-sky SW TOA flux (Figs. 7a,b), differences are generally positive over ocean. Marked differences appear in dust regions off the west coast of northern Africa (Fig. 7b) due to improvements in EBAF Ed4.0 dust/cloud discrimination: EBAF Ed4.0 values exceed Ed2.8 because Ed4.0 identifies more scenes as dust instead of cloud compared to Ed2.8. Elsewhere over the oceans, EBAF Ed4.0 exceeds Ed2.8 by $3\text{--}5 \text{ W m}^{-2}$ mainly due to the correction to a coding error found in EBAF Ed2.8 clear-sky SW TOA flux time-space averaging. In polar regions, large differences are observed primarily as a result of cloud mask differences, processing of clear-sky TOA fluxes in partly cloudy over broken sea ice, and the correction to the time-space averaging coding error in EBAF Ed2.8 (section 3a). The global average regional RMS difference is $7\text{--}8 \text{ W m}^{-2}$ in January and July (Table 6).

In contrast, the regional pattern of LW clear-sky TOA flux differences (Figs. 7c,d) shows much larger differences in regions of persistent high cloud cover, such as over the Indian Ocean, the western tropical Pacific Ocean, the ITCZ, and convective regions over the Amazon and central Africa. In some regions, differences can reach 15 W m^{-2} . The global average regional RMS difference is 4.8 W m^{-2} . For net clear-sky TOA flux, the global average regional RMS difference is 9 W m^{-2} .

With passive sensors such as MODIS, clear-sky determination over snow/ice in polar regions is recognized to be a challenge (particularly during polar night) and continues to be an active area of research (Q. Z. Trepte

TABLE 6. Bias and regional RMS difference between EBAF Ed4.0 and EBAF Ed2.8 for all-sky and clear-sky SW, LW, and net TOA flux (W m^{-2}) during January and July 2010.

	January 2010		July 2010	
	Bias	RMS	Bias	RMS
	All sky			
SW	-0.5	2.5	-0.2	2.5
LW	0.6	1.6	0.6	1.5
Net	0.5	2.9	-0.1	2.8
	Clear sky			
SW	1.5	6.9	0.4	8.0
LW	2.9	4.8	2.7	4.8
Net	-3.9	8.7	-2.7	9.2

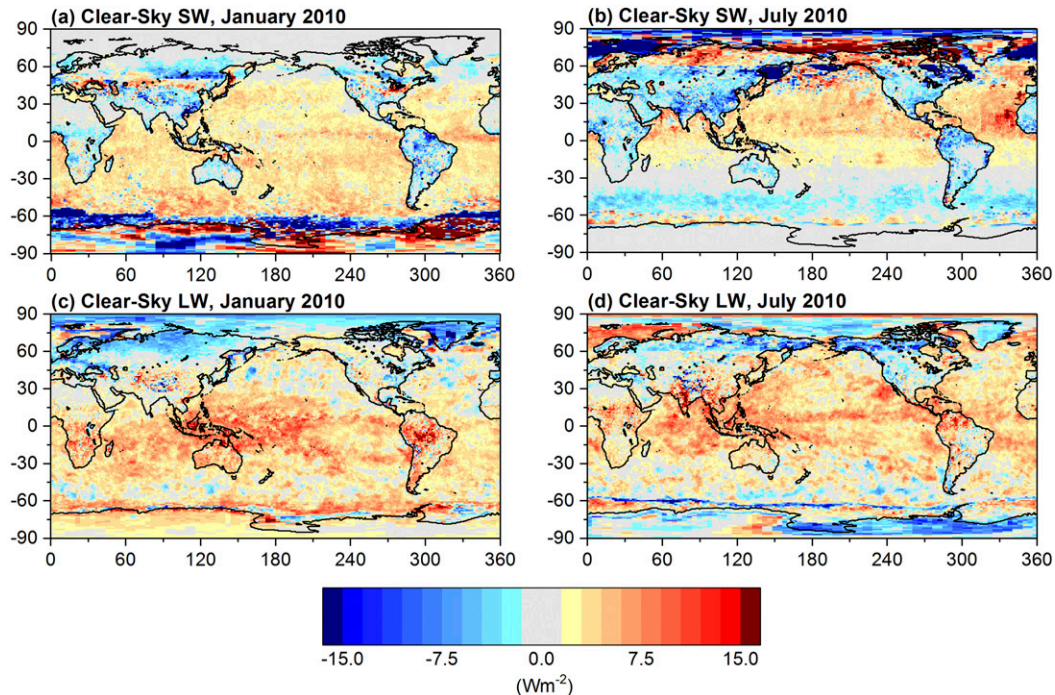


FIG. 7. EBAF Ed4.0 minus Ed2.8 clear-sky TOA flux difference in (left) January and (right) July 2010 for (a), (b) SW and (c),(d) LW fluxes.

et al. 2017, unpublished manuscript). Consequently, clear-sky TOA flux uncertainties are generally greater over the poles compared to other parts of the globe.

Regional differences in solar irradiance between EBAF Ed4.0 and Ed2.8 are shown in Figs. 8a–d for four months in 2008. The cause of the difference is in the approach used in time averaging. EBAF Ed4.0 time averaging is performed in coordinated universal time whereas EBAF Ed2.8 used local time.

d. Interannual variations and trends

In the following we examine interannual variations and trends in deseasonalized monthly anomalies in SW, LW, and net TOA fluxes for March 2000–September 2016 for EBAF Ed4.0 as well as differences between EBAF Ed4.0 and Ed2.8. The sign convention is as follows: positive anomalies in SW and LW TOA fluxes correspond to increased outgoing radiation, while positive anomalies in net TOA flux correspond to increased radiation into the earth–atmosphere system.

1) ALL SKY

Anomalies in EBAF Ed4.0 global mean all-sky TOA flux for SW, LW, and net are shown in Figs. 9a, 9c, and 9e, respectively. These anomalies reflect the influence of internal variations in the climate system, particularly that of ENSO. Positive anomalies in net TOA flux in

2008/09 are associated with La Niña conditions during most of 2008 through spring 2009. During this period, negative anomalies in both reflected SW and outgoing LW TOA flux are observed. A second period of positive net TOA flux anomalies occurring between 2011 and 2013 is associated with periods of moderate–strong La Niña conditions. Conversely, negative anomalies in net TOA flux during El Niño events in 2002/03 and 2009/10 are associated with positive anomalies in both SW and LW TOA flux. In contrast, net TOA flux anomalies are not as prominent during the 2015/16 El Niño because negative SW TOA flux anomalies are offset by positive LW TOA flux anomalies.

The large positive anomalies in SW TOA flux during the early 2000s (Fig. 9a) coincide with positive anomalies in the Arctic (Fig. 10a) as a result of greater sea ice coverage compared to the rest of the record (Hartmann and Ceppi 2014; Pistone et al. 2014), positive anomalies in the southern midlatitudes in 2002 (Fig. 10e), and positive anomalies over Antarctica in 2000 (Fig. 10f). The standard deviation in monthly anomalies (dashed lines in Figs. 9b,d,f) are 0.60, 0.51, and 0.69 W m^{-2} for SW, LW, and net TOA flux, respectively.

Anomaly differences between Ed4.0 and Ed2.8 (Figs. 9b,d,f) generally lie well within one standard deviation of Ed4.0 monthly anomalies. However, for the Terra-only period prior to 2002, EBAF Ed4.0 SW TOA

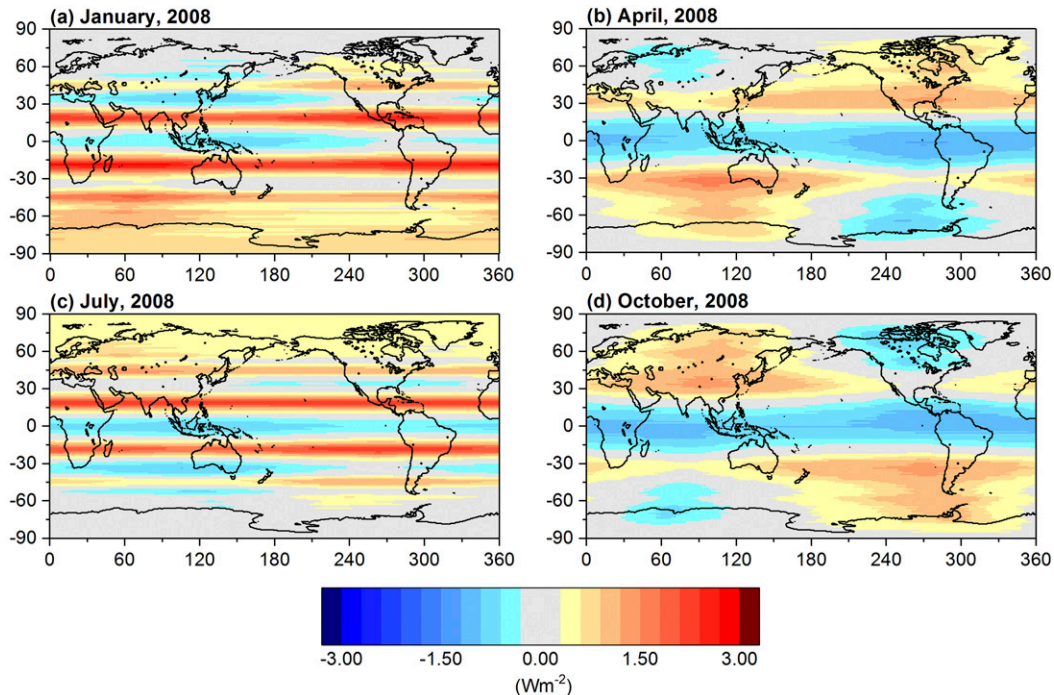


FIG. 8. Solar irradiance difference between EBAF Ed4.0 and Ed2.8 for (a) January, (b) April, (c) July, and (d) October 2008.

flux anomalies are systematically larger than Ed2.8 values by $0.3\text{--}0.4\text{ W m}^{-2}$ (Fig. 9b). While part of the reason for the difference may be related to reduced sampling during this period (Fig. 11), sampling alone cannot explain why the difference is systematic. To isolate the influence of instrument calibration differences (gains and time-dependent spectral response function changes) between Ed4.0 and Ed2.8, we compared results obtained using the same cloud retrievals, ADMs, and time interpolation methodologies, but with Ed2.8 and Ed4.0 calibration coefficients. We found SW TOA flux anomalies to be nearly identical during the *Terra*-only period. Rather, further analysis shows that the single largest contribution to the anomaly differences during the *Terra*-only period is due to the diurnal corrections used in Ed2.8. Anomalies during the *Terra*-only period from EBAF Ed2.8 are underestimated by as much as 0.2 W m^{-2} , based upon comparisons between EBAF Ed2.8 and SSF1deg-*Terra* Ed3.0. In contrast, EBAF Ed4.0 anomalies are 0.07 W m^{-2} larger than SSF1deg-*Terra* Ed4.0. However, there is also a 0.1 W m^{-2} anomaly difference during the *Terra*-only period between SSF1deg-*Terra* Ed4.0 and SSF1deg-*Terra* Ed3.0, which suggests that cloud retrieval and/or ADM differences between Ed3.0 and Ed4.0 also contribute to some of the discrepancy during the *Terra*-only period.

Figure 12a provides time series of CERES *Terra* SSF1deg Ed4A minus Ed3A SW TOA flux and MODIS-derived cloud optical depth for global ocean (note that the y axis for cloud optical depth differences has been reversed). SSF1deg Ed3A uses the same input cloud retrievals and ADMs as EBAF Ed2.8, and similarly for SSF1deg Ed4A and EBAF Ed4.0. Both SW TOA flux and cloud optical depth differences show a systematic trend of opposite sign. The two fields are strongly anti-correlated (Fig. 12b), with a correlation coefficient of -0.72 .

Deseasonalized anomalies in cloud optical depth (Fig. 13a) clearly show a much stronger decreasing trend in Ed3A than Ed4A. The reason for the cloud optical depth trend differences is due to how MODIS *Terra* calibration changes are accounted for in Ed3A and Ed4A. The *Terra*-MODIS instrument band 1 ($0.65\text{ }\mu\text{m}$) experienced two calibration anomalies over the CERES record. The first anomaly occurred on 2 July 2003 when the solar diffuser door on the *Terra*-MODIS malfunctioned and was left in the open position, causing the *Terra*-MODIS solar diffuser to degrade at a faster rate. The second anomaly occurred in early 2009, when solar diffuser degradations were observed to be 1.5% and 0.3% for *Terra*-MODIS and *Aqua*-MODIS, respectively (Wu et al. 2013). The MODIS inputs used for EBAF Ed2.8 and SSF1deg Ed3A rely on collection 4

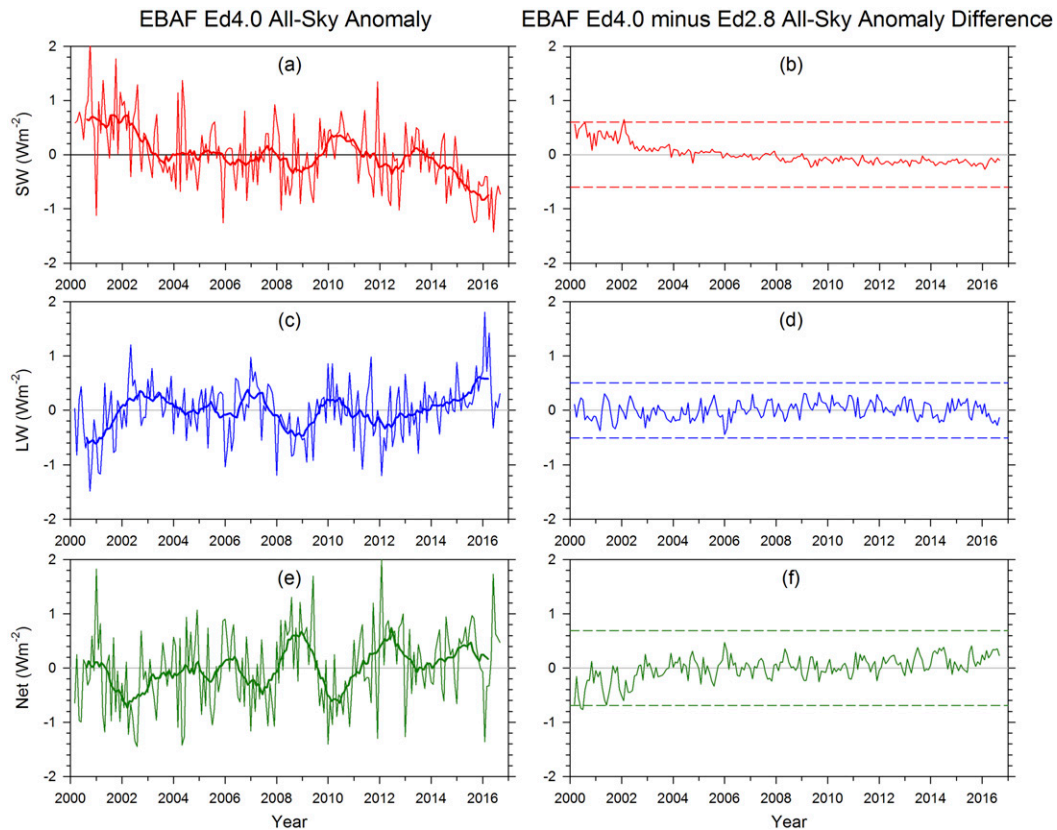


FIG. 9. Anomaly in global mean all-sky TOA flux for (left) EBAF Ed4.0 and (right) EBAF Ed4.0 minus Ed2.8 difference: (a),(b) SW, (c),(d) LW, and (e),(f) net TOA flux. Thin lines are monthly anomalies. The thick line through monthly anomalies is the 12-month running mean. Dashed lines in (b),(d),(f) are plus or minus one standard deviation in monthly anomalies from (a),(c),(e).

through April 2006 and collection 5 thereafter. CERES EBAF Ed4.0 uses collection 5 for the entire record and adjusts the MODIS collection 5 radiances to account for the *Terra*-MODIS calibration anomalies.

Because MODIS cloud optical depths are used to select anisotropic factors (i.e., ADM) in converting CERES radiances to radiative fluxes, the different cloud optical depth trends in Ed3A and Ed4A result in slightly different SW TOA flux trends as well. The Ed4-Ed3 cloud optical depth trend difference corresponds to 5% decade⁻¹ relative to the mean cloud optical depth, while the SW TOA flux trend difference corresponds to $-0.25 \text{ W m}^{-2} \text{ decade}^{-1}$.

2) CLEAR SKY

Anomalies in global mean clear-sky TOA flux for SW, LW, and net (Figs. 14a,c,e) are less variable than all sky, with standard deviations in monthly anomalies of 0.37, 0.38, and 0.51 W m^{-2} , respectively. Marked positive SW TOA flux anomalies appear in the early 2000s owing to greater Arctic sea ice coverage (noted earlier), while

negative anomalies reaching -1 W m^{-2} occur in 2016 because of reduced Arctic snow and sea ice coverage. Figures 15a-f, showing anomalies in 30° latitude zones, clearly demonstrate how variable SW TOA fluxes are in polar regions. An early 2016 retreat of sea ice in the Beaufort Sea and warm air advection into the Arctic from eastern Siberia and northern Europe led to anomalously warm conditions and below-average ice coverage (National Snow and Ice Data Center 2016). The warmer conditions are also responsible for the large positive anomalies in clear-sky LW TOA flux in 2016 (Fig. 14c).

While differences between EBAF Ed4.0 and Ed2.8 anomalies (Figs. 14b,d,f) are generally smaller than the one standard deviation in Ed4.0 monthly anomalies, there is a marked discontinuity in clear-sky LW TOA flux anomaly differences around 2008 (Fig. 14d). This is due to a change in the source of assimilated meteorological data in EBAF Ed2.8 in January 2008 from GEOS-4.1 to GEOS-5.2.0. In contrast, EBAF Ed4.0 uses GEOS-5.4.1 throughout the record.

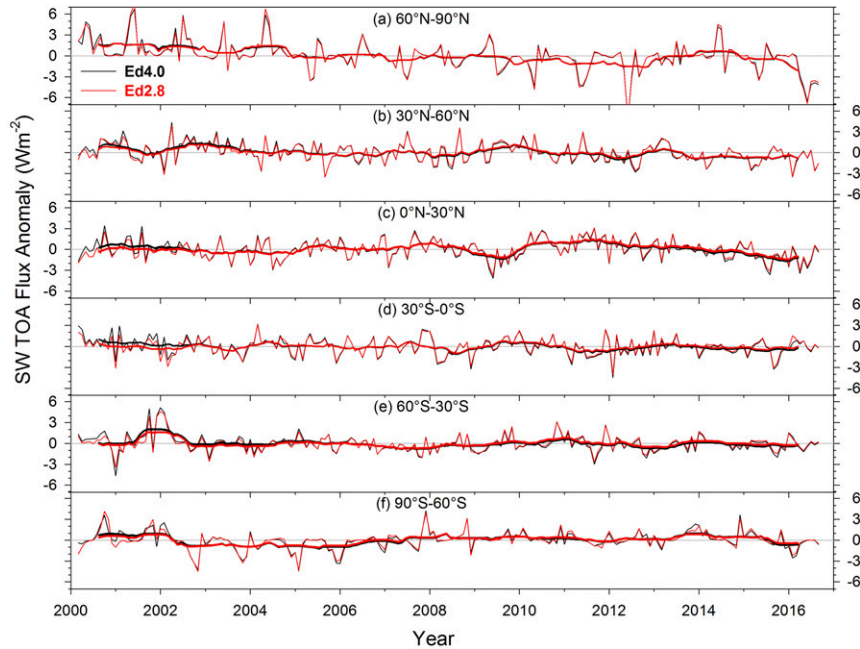


FIG. 10. EBAF Ed4.0 and Ed2.8 all-sky SW TOA flux anomalies for (a) 60°–90°N, (b) 30°–60°N, (c) 0°–30°N, (d) 30°S–0°S, (e) 60°S–30°S, and (f) 90°S–60°S. Thin lines are monthly anomalies. The thick line is a 12-month running average of monthly anomalies.

3) TRENDS

While trends in TOA flux for this short record are still primarily driven by internal variability of the climate system, it is nonetheless interesting to see how trends are influenced by the change from EBAF Ed2.8 to Ed4.0. Table 7 provides global mean trends in TOA fluxes for March 2000–September 2016 and July 2002–September 2016. In the SW, both all-sky and clear-sky TOA flux trends are negative and either exceed or are close to the 95% significance level. In contrast, all-sky LW TOA flux trends are $<0.2 \text{ W m}^{-2} \text{ decade}^{-1}$. EBAF Ed4.0 clear-sky LW trends are near zero, whereas Ed2.8 shows trends of approximately $-0.3 \text{ W m}^{-2} \text{ decade}^{-1}$. In the SW, the largest discrepancy between EBAF Ed2.8 and Ed4.0 is for all-sky during March 2000–September 2016. This is

mainly related to the larger SW anomaly differences during the *Terra*-only period, as discussed in section 3d(1).

4. TOA flux uncertainty

In the following, we estimate uncertainties in $1^\circ \times 1^\circ$ regional monthly SW, LW, and net TOA flux for all sky, clear sky, and CRE. To determine the total SW and LW flux uncertainties, we include all known sources of uncertainty and combine them assuming they are independent, so the total uncertainty is given by the square root of the sum-of-squares of the individual contributions. For net TOA flux, we also assume no correlation between SW and LW uncertainties. As described further in section 4e, the

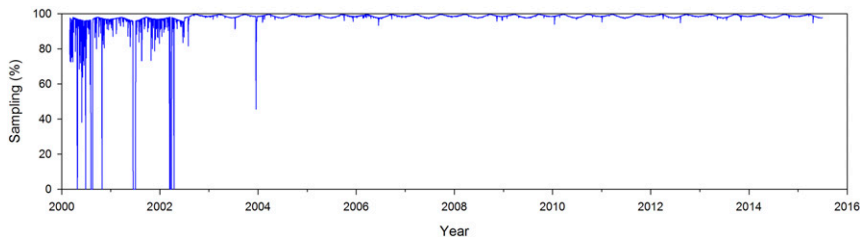


FIG. 11. Spatial sampling for SSF1deg daily input files used to determine EBAF Ed4.0 monthly means. Sampling is defined as the area-weighted percentage of the globe with valid daily mean SW and LW TOA flux values on a given day.

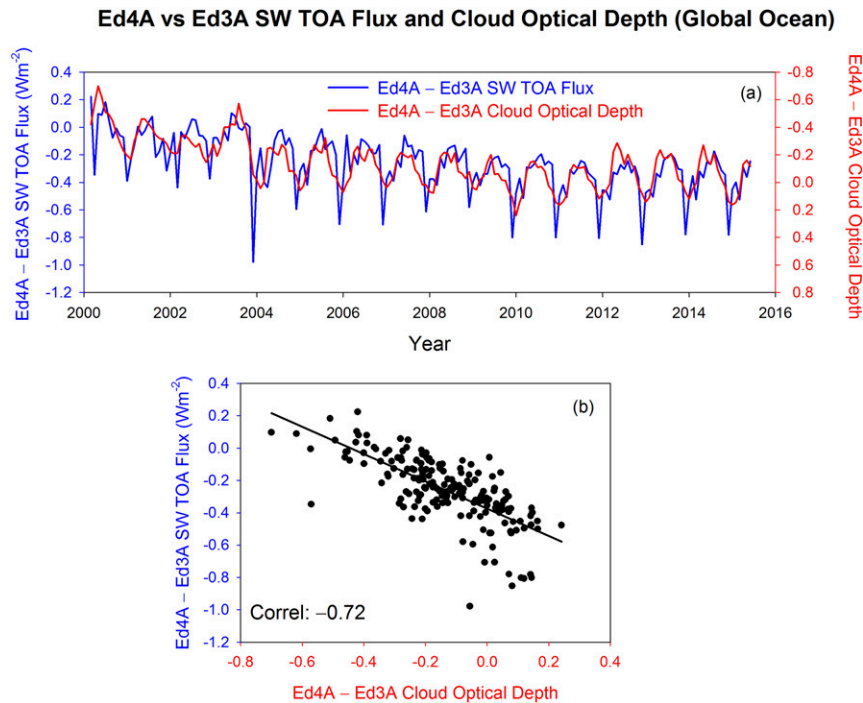


FIG. 12. (a) Time series of SSF1deg Ed4A minus Ed3A SW TOA flux and cloud optical depth for global ocean. (b) Scatterplot of time series shown in (a), with regression line and correlation shown at the bottom left.

correlation between calibration uncertainties for all-sky and clear-sky TOA fluxes is accounted for in determining the uncertainty in CRE. Table 8 summarizes the regional uncertainties separately for the *Terra*-only (March 2000–June 2002) and *Terra-Aqua* (July 2002 onward) periods.

a. All-sky SW TOA flux

We assume the overall uncertainty is due to 1) the EBAF diurnal correction, 2) radiance-to-flux conversion error (Su et al. 2015b), and 3) CERES instrument calibration uncertainty. The EBAF diurnal correction

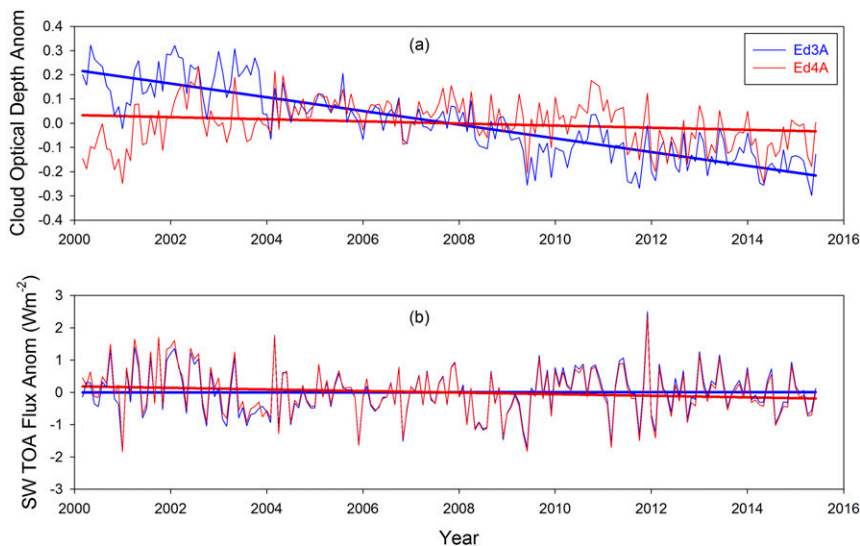


FIG. 13. (a) Time series of SSF1deg Ed3A and Ed4A anomalies in (a) cloud optical depth and (b) SW TOA flux for global ocean. Thick straight lines are least squares regression fits to the monthly anomalies.

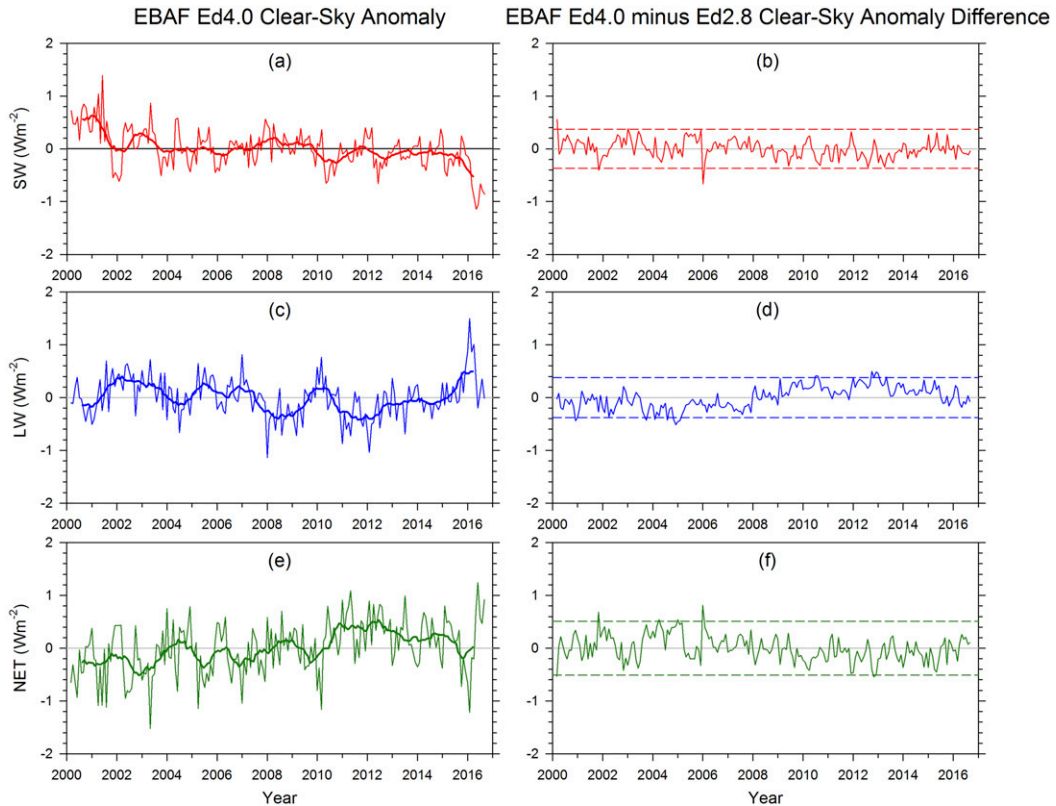


FIG. 14. As in Fig. 9, but for anomaly in global mean clear-sky TOA flux.

uncertainty is 2.7 W m^{-2} for the *Terra*-only period and 1.9 W m^{-2} for the *Terra-Aqua* period [section 2b(1)]. According to Su et al. (2015b), radiance-to-flux conversion error is 1 W m^{-2} , and CERES instrument calibration uncertainty is 1 W m^{-2} (1σ). Therefore, the overall regional monthly uncertainty is $(2.7^2 + 1^2 + 1^2)^{1/2}$ or approximately 3 W m^{-2} for the *Terra*-only period and $(1.9^2 + 1^2 + 1^2)^{1/2}$ or approximately 2.5 W m^{-2} for the *Terra-Aqua* period.

We note that these are overall uncertainties and are not necessarily representative of all regions. For example, in areas with strong diurnal cycles such as the stratocumulus regions (Figs. 5c,d), errors can reach $5\text{--}10 \text{ W m}^{-2}$ for the *Terra*-only period and $3\text{--}7 \text{ W m}^{-2}$ for the *Terra-Aqua* period.

b. All-sky LW TOA flux

To determine uncertainties resulting from temporal interpolation for the *Terra*-only period, we use data from the *Terra-Aqua* period and compare regional fluxes between SSF1deg-*Terra* with regional fluxes in SYN1deg-*Terra-Aqua*. In SSF1deg, linear temporal interpolation between CERES observations is used over ocean whereas a one-half sine fit is applied over

land to account for daytime heating. Temporal interpolation uncertainties for the *Terra-Aqua* period are determined by comparing regional fluxes from SSF1deg-*Terra-Aqua* with SYN1deg-*Terra-Aqua*. As noted in section 2b(1), EBAF all-sky LW TOA fluxes are derived from SYN1deg values. Therefore, differences between SSF1deg and SYN1deg are likely an upper bound on temporal interpolation uncertainties. Results for the *Terra*-only period are shown in Fig. 16a for October 2008. LW TOA flux differences are generally less than 5 W m^{-2} except over Tibet, convective regions in central Africa, and mountainous regions in South America. The errors are markedly reduced when both *Terra* and *Aqua* are used in SSF1deg (Fig. 16b). The overall RMS error between 60°S and 60°N is 2.2 W m^{-2} for the *Terra*-only case and 1.4 W m^{-2} when *Terra* and *Aqua* are combined.

If we assume the overall uncertainty is due to 1) the EBAF diurnal correction, 2) radiance-to-flux conversion error of 0.75 W m^{-2} (Su et al. 2015b), and 3) CERES instrument calibration uncertainty of 0.75% or 1.8 W m^{-2} (1σ), the regional monthly uncertainty of all-sky LW TOA flux for EBAF Ed4.0 for March 2000–June 2002 is estimated as $(2.2^2 + 0.75^2 + 1.8^2)^{1/2}$ or approximately 3 W m^{-2} , and for July 2002 onward it is

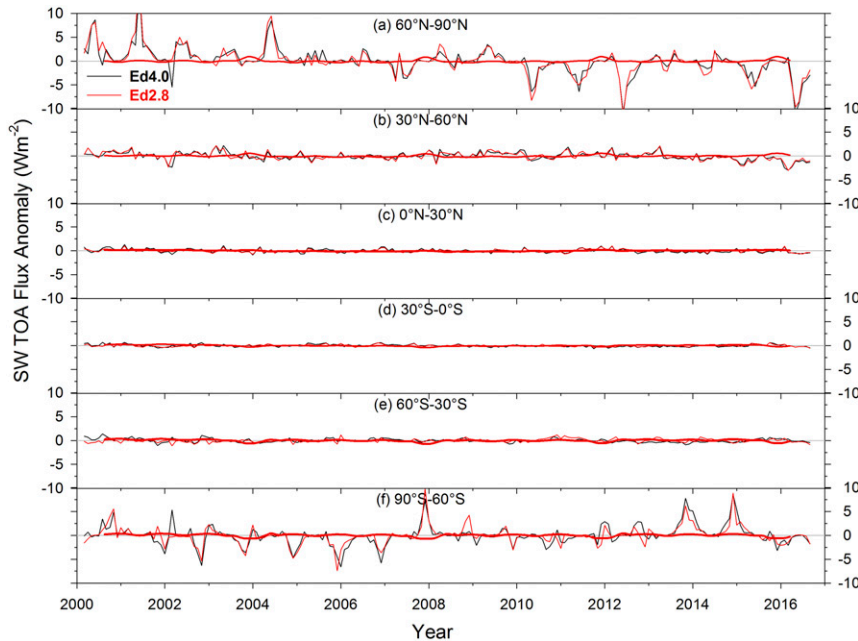


FIG. 15. As in Fig. 10, but for clear-sky SW TOA flux anomalies.

estimated as $(1.4^2 + 0.75^2 + 1.8^2)^{1/2}$ or approximately 2.5 W m^{-2} .

c. Clear-sky SW TOA flux

The uncertainty in $1^\circ \times 1^\circ$ regional monthly clear-sky SW TOA flux is determined from calibration uncertainty, errors in narrowband-to-broadband conversion, radiance-to-flux conversion, time-space averaging, and scene identification. During the *Terra*-only period, there is also uncertainty resulting from the adjustment made to *Terra* clear-sky TOA fluxes, applied to ensure that *Terra* clear-sky fluxes prior to July 2002 are consistent with those from *Aqua* after July 2002, thereby minimizing possible discontinuities between the *Terra*-only and *Terra-Aqua* periods.

For CERES, calibration uncertainty is 1% (1σ), which for a typical global mean clear-sky SW flux corresponds to

approximately 0.5 W m^{-2} . The narrowband-to-broadband regional RMS error is 0.9 W m^{-2} , determined by applying the narrowband-to-broadband regressions to cloud-free CERES footprints and comparing with CERES radiances. For clear-sky SW TOA flux, the radiance-to-flux conversion error contributes 1 W m^{-2} to regional RMS error (Loeb et al. 2007), and time-space averaging adds 2 W m^{-2} uncertainty. The latter is based upon an estimate of the error from TRMM-derived diurnal albedo models that provide albedo dependence upon scene type (Loeb et al. 2003).

In EBAF, “clear sky” is defined as cloud free at the MODIS pixel scale (1 km). A pixel is identified as clear using spectral MODIS channel information and a cloud mask algorithm (Q. Z. Trepte et al. 2017, unpublished manuscript). Uncertainty resulting from the cloud mask algorithm is 4 W m^{-2} based upon a comparison of clear-sky

TABLE 7. Global mean TOA flux/CRE trend ($\text{W m}^{-2} \text{ decade}^{-1}$) for March 2000–September 2016 and July 2002–September 2016. Uncertainties are at the 95% significance level and only account for interannual variations in monthly anomalies.

	All sky		Clear sky		CRE	
	Ed2.8	Ed4.0	Ed2.8	Ed4.0	Ed2.8	Ed4.0
March 2000–September 2016						
SW	-0.26 ± 0.18	-0.57 ± 0.19	-0.27 ± 0.16	-0.36 ± 0.17	-0.004 ± 0.19	0.21 ± 0.22
LW	0.14 ± 0.21	0.19 ± 0.21	-0.31 ± 0.26	-0.07 ± 0.20	-0.45 ± 0.10	-0.26 ± 0.11
Net	0.09 ± 0.23	0.35 ± 0.24	0.55 ± 0.19	0.40 ± 0.20	-0.45 ± 0.23	-0.05 ± 0.22
July 2002–September 2016						
SW	-0.20 ± 0.23	-0.39 ± 0.23	-0.17 ± 0.19	-0.28 ± 0.20	0.03 ± 0.23	0.11 ± 0.25
LW	0.04 ± 0.25	0.09 ± 0.24	-0.33 ± 0.34	-0.05 ± 0.25	-0.37 ± 0.12	-0.14 ± 0.11
Net	0.23 ± 0.28	0.36 ± 0.31	0.57 ± 0.23	0.40 ± 0.25	-0.34 ± 0.30	-0.04 ± 0.28

TABLE 8. Uncertainty in $1^\circ \times 1^\circ$ regional monthly TOA flux and CRE for SW, LW, and net (W m^{-2}). Separate uncertainties are provided for the *Terra-only* and *Terra-Aqua* periods.

	All sky	Clear sky	CRE
		<i>Terra-only period</i>	
SW	3	6	6.6
LW	3	5	5.2
Net	4.2	7.8	8.4
		<i>Terra-Aqua period</i>	
SW	2.5	5	5.5
LW	2.5	4.5	4.4
Net	3.5	6.7	7

SW TOA fluxes for the Ed4.0 cloud mask and that used in Ed3.0. In addition, there is scene misclassification due to subvisual cirrus. From a comparison of SW TOA fluxes for CERES footprints identified as clear according to MODIS but cloudy according to *CALIPSO* with TOA fluxes from footprints identified as clear according to both MODIS and *CALIPSO*, Sun et al. (2011) found that footprints with undetected subvisual clouds reflect 2.5 W m^{-2} more SW radiation compared to completely cloud-free footprints and occur in approximately 50% of footprints identified as clear by MODIS. This implies an error of 1.25 W m^{-2} because of misclassification of clear scenes. For the *Terra-Aqua* period, the total error in TOA outgoing clear-sky SW radiation in a region is estimated as $(0.5^2 + 0.9^2 + 1^2 + 2^2 + 4^2 + 1.25^2)^{1/2}$ or approximately 5 W m^{-2} . For the *Terra-only* period, the uncertainty resulting from the adjustment made to *Terra* clear-sky TOA fluxes is determined by comparing the adjusted *Terra* clear-sky TOA fluxes with corresponding *Aqua* values. For March 2003, the regional RMS was 3 W m^{-2} (other months give similar results). Thus, for the *Terra-only* period, the total error in TOA outgoing clear-sky SW radiation in a region is $(0.5^2 + 0.9^2 + 1^2 + 2^2 + 4^2 + 1.25^2 + 3.0^2)^{1/2}$ or approximately 6 W m^{-2} .

d. Clear-sky LW TOA flux

For CERES, LW calibration uncertainty is 0.75% (1σ), which for a typical global mean clear-sky LW flux corresponds to approximately 2 W m^{-2} . The narrowband-to-broadband regional RMS error is 1.6 W m^{-2} , determined by applying the narrowband-to-broadband regressions to cloud-free CERES footprints and comparing with CERES radiances. For clear-sky LW TOA flux, the radiance-to-flux conversion error contributes 0.7 W m^{-2} to regional RMS error (Loeb et al. 2009), and time-space averaging adds 1 W m^{-2} uncertainty. The latter assumes zero error over ocean (i.e., no appreciable diurnal cycle in clear-sky LW flux) and a 3 W m^{-2} error in the one-half sine fit over land and desert (Young et al. 1998). Uncertainty resulting from the cloud mask algorithm is

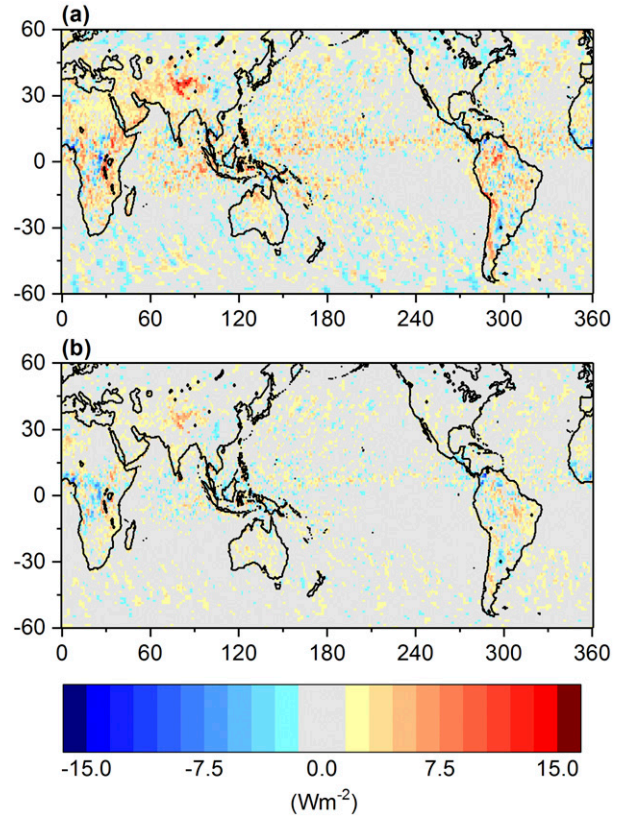


FIG. 16. All-sky LW TOA flux difference relative to SYN1deg-*Terra-Aqua* for (a) SSF1deg-*Terra* and (b) SSF1deg-*Terra-Aqua* for October 2008.

3 W m^{-2} based upon a comparison of clear-sky LW TOA fluxes for the Ed4.0 cloud mask and that used in Ed3.0. Sun et al. (2011) found that footprints with undetected subvisual clouds emit 5.5 W m^{-2} less LW radiation compared to completely cloud-free footprints and occur in approximately 50% of footprints identified as clear by MODIS. This implies an error of 2.75 W m^{-2} because of misclassification of clear scenes.

The total error in TOA outgoing clear-sky LW radiation in a region is estimated as $(2^2 + 1.6^2 + 0.7^2 + 1^2 + 3^2 + 2.75^2)^{1/2}$ or approximately 4.5 W m^{-2} . For the *Terra-only* period, the regional RMS uncertainty resulting from the adjustment made to *Terra* clear-sky TOA fluxes is 1.8 W m^{-2} for March 2003 (other months give similar results). Thus for the *Terra-only* period, the total error in TOA outgoing clear-sky LW radiation in a region is $(2^2 + 1.6^2 + 0.7^2 + 1^2 + 2.75^2 + 3^2 + 1.8^2)^{1/2}$ or approximately 5 W m^{-2} .

e. CRE

Because CRE is a difference between all-sky and clear-sky TOA fluxes, and because the same calibration coefficients are used to determine both, we cannot

assume the all-sky and clear-sky uncertainties [$U(\text{all sky})$ and $U(\text{clear sky})$, respectively] are independent. Accordingly, we determine the uncertainty in CRE accounting for the correlation in calibration uncertainty U_{CAL} for clear and all sky as follows:

$$U(\text{CRE}) = [U(\text{all sky})^2 + U(\text{clear sky})^2 - 2U_{\text{CAL}}(\text{all sky})U_{\text{CAL}}(\text{clear sky})]^{1/2} \quad (2)$$

As shown in Table 8, after accounting for the correlation, CRE uncertainties are very similar to those for clear-sky TOA flux, especially in the LW. Overall, net CRE uncertainties are a factor of 2 larger than those for all-sky TOA fluxes.

5. Summary

The goal of the CERES project is to produce a long-term integrated global climate data record of Earth's radiation budget in order to quantify its variability over a range of time and space scales. This is achieved by combining CERES broadband measurements with MODIS and geostationary imager data to provide a diurnally complete representation of Earth's radiation budget. This paper describes the EBAF-TOA Ed4.0 data product, which consists of monthly mean SW, LW, and net TOA all-sky and clear-sky radiative fluxes over $1^\circ \times 1^\circ$ latitude–longitude regions. Also included in EBAF-TOA Ed4.0 are MODIS-based cloud properties (cloud amount, optical depth, effective pressure, and temperature at cloud top).

Uncertainties in absolute calibration and the algorithms used to determine Earth's radiation budget from satellite measurements are too large to enable Earth's energy imbalance to be quantified in an absolute sense. Rather the CERES data products are more useful for providing its spatial and temporal variability. The absolute value of global and regional mean net TOA flux is nevertheless important in many applications that use ERB data (e.g., climate model evaluation). To produce a globally complete representation of ERB while at the same time providing representative absolute values, the EBAF data product uses an objective constraint algorithm to adjust SW and LW TOA fluxes within their range of uncertainty to remove the inconsistency between average global net TOA flux and EEI as inferred from in situ data. According to Johnson et al. (2016), Earth's energy imbalance during July 2005–June 2015 is $0.71 \pm 0.10 \text{ W m}^{-2}$ (uncertainties at the 95% confidence level).

To resolve the diurnal cycle of clouds and radiation between CERES observation times, the CERES SYN1deg data product merges CERES and 1-hourly GEO data. However, artifacts in the GEO imager visible

bands over certain regions and time periods can introduce larger regional uncertainties. Spurious jumps in the SW TOA flux record can occur when GEO satellites are replaced, because of changes in satellite position, calibration, visible sensor spectral response, cloud retrieval quality, and imaging schedules. Such artifacts in the GEO data can be problematic in studies of TOA radiation interannual variability and/or trends. To ensure EBAF-TOA maintains the excellent radiometric stability of CERES and also preserves the diurnal information found in SYN1deg, EBAF Ed4.0 uses a new approach involving empirical diurnal correction ratios to convert daily regional mean SSF1deg SW fluxes to diurnally complete values analogous to SYN1deg, but without GEO artifacts. In the LW, the problem is less severe as the GEO imager infrared bands are generally stable owing to the availability of onboard blackbody sources for calibration. Therefore, LW monthly mean TOA fluxes are computed directly from SYN1deg daily mean LW TOA fluxes.

Clear-sky regional maps constructed from cloud-free CERES footprints ($\sim 20 \text{ km}$ at nadir) contain many gaps in cloudy regions even at monthly time scales. To increase sampling, we supplement the CERES clear-sky fluxes with TOA fluxes inferred from MODIS radiances within clear portions of CERES footprints. This involves developing and applying a CERES–MODIS narrowband-to-broadband radiance conversion algorithm and then inferring TOA flux from the MODIS “broadband” radiances using the same CERES algorithms. The resulting clear-sky maps are largely gap free following this procedure.

EBAF Ed4.0 all-sky global mean TOA radiative fluxes exceed EBAF Ed2.8 by 0.5 W m^{-2} in the LW but are 0.5 W m^{-2} smaller in the SW. Differences are much greater for clear sky, with EBAF Ed4.0 exceeding Ed2.8 by 2.7 W m^{-2} in the LW and 0.8 W m^{-2} in the SW. Because of the large clear-sky differences, EBAF Ed4.0 net CRE is -18 W m^{-2} compared to -21 W m^{-2} for EBAF Ed2.8. Regionally, EBAF Ed4.0 all-sky TOA fluxes exceed Ed2.8 by up to 7.5% over marine stratocumulus regions owing to algorithm improvements in the diurnal correction methodology and increased sampling of the diurnal cycle with 1-hourly instead of 3-hourly GEO imager data. The global mean regional RMS difference is 2.5 W m^{-2} in the SW and 1.5 W m^{-2} in the LW. For clear sky, marked positive differences between EBAF Ed4.0 and Ed2.8 SW TOA flux occurs in dust regions (off the coast of northern Africa) due to improvements in the MODIS dust/cloud mask in Ed4.0. EBAF Ed4.0 SW TOA fluxes exceed Ed2.8 values by $3\text{--}5 \text{ W m}^{-2}$ over ocean due to a coding error found in Ed2.8 time–space averaging, which has been corrected in Ed4.0. Large SW TOA flux differences also occur in polar regions as a result of cloud mask differences, improvements in how clear-sky TOA fluxes are processed in partly cloudy

conditions over broken sea ice, and the correction to the Ed2.8 time-space averaging coding error. The global average regional RMS difference between EBAF Ed4.0 and Ed2.8 clear-sky SW TOA flux is 8 W m^{-2} . In the LW, EBAF Ed4.0 clear-sky TOA fluxes exceed EBAF Ed2.8, especially in regions of persistent high cloud cover. The global average regional RMS difference for clear-sky LW flux is 4.8 W m^{-2} .

CERES TOA fluxes exhibit pronounced interannual variability driven primarily by ENSO. SW TOA flux variations in the Arctic are noteworthy and are tied to changes in sea ice coverage. The largest differences between EBAF Ed4.0 and Ed2.8 anomalies occur for SW all-sky flux during the *Terra*-only period, with EBAF Ed4.0 anomalies exceeding Ed2.8 by $0.3\text{--}0.4 \text{ W m}^{-2}$. The cause is primarily due to a bias in the diurnal models used in EBAF Ed2.8, which is removed in Ed4.0. In addition, pronounced cloud optical depth retrieval differences occurring as a result of a correction to MODIS calibration changes in Ed4.0 accounts for some of the difference. Because MODIS cloud optical depths are used to select anisotropic factors for radiance-to-flux conversion, large swings in cloud optical depth can impact SW TOA fluxes too.

We estimate the uncertainty in $1^\circ \times 1^\circ$ latitude-longitude regional monthly mean all-sky TOA flux to be 3 W m^{-2} (1σ) for the *Terra*-only period and 2.5 W m^{-2} for the *Terra-Aqua* period both for SW and LW. For clear sky, uncertainties are larger owing primarily to the need to use a cloud mask to distinguish between clear and cloudy regions. The SW clear-sky regional uncertainty is estimated to be 6 W m^{-2} for the *Terra*-only period and 5 W m^{-2} for the *Terra-Aqua* period. In the LW, the regional monthly uncertainty is 5 W m^{-2} for *Terra*-only and 4.5 W m^{-2} for *Terra-Aqua*.

Acknowledgments. This research has been supported by the NASA CERES project. (The CERES EBAF Ed4.0 dataset was downloaded from <https://ceres-tool.larc.nasa.gov/ord-tool/jsp/EBAF4Selection.jsp>.) The NASA Langley Atmospheric Sciences Data Center processed the instantaneous Single Scanner Footprint (SSF) data used as input to EBAF Ed4.0. Some of the material in this paper is reproduced from the CERES Data Quality Summaries for Edition 2.8 and Edition 4.0 (available online at https://ceres.larc.nasa.gov/documents/DQ_summaries/CERES_EBAF_Ed2.8_DQS.pdf and https://ceres.larc.nasa.gov/documents/DQ_summaries/CERES_EBAF_Ed4.0_DQS.pdf). The authors thank the editor, Dr. Karen Shell, and three anonymous reviewers for their helpful comments and suggestions.

REFERENCES

- Abraham, J. P., and Coauthors, 2013: A review of global ocean temperature observations: implications for ocean heat content estimates and climate change. *Rev. Geophys.*, **51**, 450–483, <https://doi.org/10.1002/rog.20022>.
- Chang, F.-L., P. Minnis, B. Lin, M. M. Khaiyer, R. Palikonda, and D. A. Spangenberg, 2010: A modified method for inferring upper troposphere cloud top height using the GOES 12 imager 10.7 and 13.3 μm data. *J. Geophys. Res.*, **115**, D06208, <https://doi.org/10.1029/2009JD012304>.
- Dewitte, S. 2013: The contribution of the DIARAD type radiometer to the revision of the solar constant. RMIB Tech. Note, 8 pp., ftp://gerb.oma.be/steven/RMIB_TSI_composite/diaradnewsolarconstant.pdf.
- , D. Crommelynck, S. Mekouari, and A. Joukoff, 2004: Measurement and uncertainty of the long-term total solar irradiance trend. *Sol. Phys.*, **224**, 209–216, <https://doi.org/10.1007/s11207-005-5698-7>.
- Doelling, D. R., and Coauthors, 2013: Geostationary enhanced temporal interpolation for CERES flux products. *J. Atmos. Oceanic Technol.*, **30**, 1072–1090, <https://doi.org/10.1175/JTECH-D-12-00136.1>.
- , M. Sun, L. T. Nguyen, M. L. Nordeen, C. O. Haney, D. F. Keyes, and P. E. Mlynchak, 2016: Advances in geostationary-derived longwave fluxes for the CERES synoptic (SYN1deg) product. *J. Atmos. Oceanic Technol.*, **33**, 503–521, <https://doi.org/10.1175/JTECH-D-15-0147.1>.
- Hansen, J., M. Sato, P. Kharecha, and K. von Schuckmann, 2011: Earth's energy imbalance and implications. *Atmos. Chem. Phys.*, **11**, 13 421–13 449, <https://doi.org/10.5194/acp-11-13421-2011>.
- Hartmann, D. L., and P. Ceppi, 2014: Trends in the CERES dataset, 2000–13: The effects of sea ice and jet shifts and comparison to climate models. *J. Climate*, **27**, 2444–2456, <https://doi.org/10.1175/JCLI-D-13-00411.1>.
- Hsu, N. C., S.-C. Tsay, M. D. King, and J. R. Herman, 2004: Aerosol properties over bright-reflecting source regions. *IEEE Trans. Geosci. Remote Sens.*, **42**, 557–569, <https://doi.org/10.1109/TGRS.2004.824067>.
- , —, and —, 2006: Deep blue retrievals of Asian aerosol properties during ACE-Asia. *IEEE Trans. Geosci. Remote Sens.*, **44**, 3180–3195, <https://doi.org/10.1109/TGRS.2006.879540>.
- Johnson, G. C., J. M. Lyman, and N. G. Loeb, 2016: Improving estimates of Earth's energy imbalance. *Nat. Climate Change*, **6**, 639–640, <https://doi.org/10.1038/nclimate3043>.
- Kato, S., and N. G. Loeb, 2003: Twilight irradiance reflected by the earth estimated from Clouds and the Earth's Radiant Energy System (CERES) measurements. *J. Climate*, **16**, 2646–2650, [https://doi.org/10.1175/1520-0442\(2003\)016<2646:TIRBTE>2.0.CO;2](https://doi.org/10.1175/1520-0442(2003)016<2646:TIRBTE>2.0.CO;2).
- , —, F. G. Rose, D. R. Doelling, D. A. Rutan, T. E. Caldwell, L. Yu, and R. A. Weller, 2013: Surface irradiances consistent with CERES-derived top-of-atmosphere shortwave and longwave irradiances. *J. Climate*, **26**, 2719–2740, <https://doi.org/10.1175/JCLI-D-12-00436.1>.
- Kopp, G., and J. L. Lean, 2011: A new, lower value of total solar irradiance: Evidence and climate significance. *Geophys. Res. Lett.*, **38**, L01706, <https://doi.org/10.1029/2010GL045777>.
- Levy, R. C., S. Mattoo, L. A. Munchak, L. A. Remer, A. M. Sayer, F. Patadia, and N. C. Hsu, 2013: The collection 6 MODIS aerosol products over land and ocean. *Atmos. Meas. Tech.*, **6**, 2989–3034, <https://doi.org/10.5194/amt-6-2989-2013>.
- Loeb, N. G., K. J. Priestley, D. P. Kratz, E. B. Geier, R. N. Green, B. A. Wielicki, P. O. Hinton, and S. K. Nolan, 2001: Determination of unfiltered radiances from the Clouds and the Earth's Radiant Energy System (CERES) instrument. *J. Appl. Meteor.*, **40**, 822–835, [https://doi.org/10.1175/1520-0450\(2001\)040<0822:DOURFT>2.0.CO;2](https://doi.org/10.1175/1520-0450(2001)040<0822:DOURFT>2.0.CO;2).

- , S. Kato, and B. A. Wielicki, 2002: Defining top-of-the-atmosphere flux reference level for earth radiation budget studies. *J. Climate*, **15**, 3301–3309, [https://doi.org/10.1175/1520-0442\(2002\)015<3301:DTOTAF>2.0.CO;2](https://doi.org/10.1175/1520-0442(2002)015<3301:DTOTAF>2.0.CO;2).
- , N. Manalo-Smith, S. Kato, W. F. Miller, S. K. Gupta, P. Minnis, and B. A. Wielicki, 2003: Angular distribution models for top-of-atmosphere radiative flux estimation from the Clouds and the Earth's Radiant Energy System instrument on the Tropical Rainfall Measuring Mission satellite. Part I: Methodology. *J. Appl. Meteor.*, **42**, 240–265, [https://doi.org/10.1175/1520-0450\(2003\)042<0240:ADMFTO>2.0.CO;2](https://doi.org/10.1175/1520-0450(2003)042<0240:ADMFTO>2.0.CO;2).
- , and Coauthors, 2007: Multi-instrument comparison of top-of-atmosphere reflected solar radiation. *J. Climate*, **20**, 575–591, <https://doi.org/10.1175/JCLI4018.1>.
- , B. A. Wielicki, D. R. Doelling, G. L. Smith, D. F. Keyes, S. Kato, N. Manalo-Smith, and T. Wong, 2009: Toward optimal closure of the Earth's top-of-atmosphere radiation budget. *J. Climate*, **22**, 748–766, <https://doi.org/10.1175/2008JCLI2637.1>.
- , J. M. Lyman, G. C. Johnson, R. P. Allan, D. R. Doelling, T. Wong, B. J. Soden, and G. L. Stephens, 2012: Observed changes in top-of-the-atmosphere radiation and upper-ocean heating consistent within uncertainty. *Nat. Geosci.*, **5**, 110–113, <https://doi.org/10.1038/ngeo1375>.
- , N. Manalo-Smith, W. Su, M. Shankar, and S. Thomas, 2016: CERES top-of-atmosphere earth radiation budget climate data record: Accounting for in-orbit changes in instrument calibration. *Remote Sens.*, **8**, 182, <https://doi.org/10.3390/rs8030182>.
- Lyman, J. M., and G. C. Johnson, 2008: Estimating annual global upper-ocean heat content anomalies despite irregular in situ ocean sampling. *J. Climate*, **21**, 5629–5641, <https://doi.org/10.1175/2008JCLI2259.1>.
- Mekaoui, S., and S. Dewitte, 2008: Total solar irradiance measurement and modelling during cycle 23. *Sol. Phys.*, **247**, 203–216, <https://doi.org/10.1007/s11207-007-9070-y>.
- National Snow and Ice Data Center, 2016: Low ice, low snow, both poles. NSIDC Arctic Sea Ice News & Analysis, <https://nsidc.org/arcticseaicenews/2016/06/>.
- Pistone, K., I. Eisenman, and V. Ramanathan, 2014: Observational determination of albedo decrease caused by vanishing Arctic sea ice. *Proc. Natl. Acad. Sci. USA*, **111**, 3322–3326, <https://doi.org/10.1073/pnas.1318201111>.
- Purkey, S. G., and G. C. Johnson, 2010: Warming of global abyssal and deep southern ocean waters between the 1990s and 2000s: Contributions to global heat and sea level rise budgets. *J. Climate*, **23**, 6336–6351, <https://doi.org/10.1175/2010JCLI3682.1>.
- Raschke, E., S. Kinne, W. B. Rossow, P. W. Stackhouse Jr., and M. Wild, 2016: Comparison of radiative energy flows in observational datasets and climate modeling. *J. Appl. Meteor. Climatol.*, **55**, 93–117, <https://doi.org/10.1175/JAMC-D-14-0281.1>.
- Remer, L. A., and Coauthors, 2008: Global aerosol climatology from the MODIS satellite sensors. *J. Geophys. Res.*, **113**, D14S07, <https://doi.org/10.1029/2007JD009661>.
- Rhein, M., and Coauthors, 2013: Observations: Ocean. *Climate Change 2013: The Physical Science Basis*, T. F. Stocker et al., Eds., Cambridge University Press, 255–315.
- Rienecker, M. M., and Coauthors, 2008: The GOES-5 Data Assimilation System—Documentation of versions 5.0.1, 5.1.0, and 5.2.0. NASA Tech. Rep. Series on Global Modeling and Data Assimilation, Vol. 27, NASA/TM-2008-105606, 97 pp.
- Roemmich, D., and Coauthors, 2009: Argo: The challenge of continuing 10 years of progress. *Oceanography*, **22**, 46–55, <https://doi.org/10.5670/oceanog.2009.65>.
- Rutan, D. A., S. Kato, D. R. Doelling, F. G. Rose, L. T. Nguyen, T. E. Caldwell, and N. G. Loeb, 2015: CERES synoptic product: Methodology and validation of surface radiant flux. *J. Atmos. Oceanic Technol.*, **32**, 1121–1143, <https://doi.org/10.1175/JTECH-D-14-00165.1>.
- Sohn, B.-J., J. Schmetz, R. Stuhlmann, and J.-Y. Lee, 2006: Dry bias in satellite-derived clear-sky water vapor and its contribution to longwave cloud radiative forcing. *J. Climate*, **19**, 5570–5580, <https://doi.org/10.1175/JCLI3948.1>.
- Stephens, G. L., D. O'Brien, P. J. Webster, P. Pilewski, S. Kato, and J.-L. Li, 2015: The albedo of Earth. *Rev. Geophys.*, **53**, 141–163, <https://doi.org/10.1002/2014RG000449>.
- Su, W., J. Corbett, Z. Eitzen, and L. Liang, 2015a: Next-generation angular distribution models for top-of-atmosphere radiative flux calculation from CERES instruments: Methodology. *Atmos. Meas. Tech.*, **8**, 611–632, <https://doi.org/10.5194/amt-8-611-2015>.
- , —, —, and —, 2015b: Next-generation angular distribution models for top-of-atmosphere radiative flux calculation from CERES instruments: Validation. *Atmos. Meas. Tech.*, **8**, 3297–3313, <https://doi.org/10.5194/amt-8-3297-2015>.
- Sun, J., X. Xiong, Y. Li, S. Madhavan, A. Wu, and B. N. Wenny, 2014: Evaluation of radiometric improvements with electronic crossstalk correction for Terra MODIS band 27. *IEEE Trans. Geosci. Remote Sens.*, **52**, 6497–6507, <https://doi.org/10.1109/TGRS.2013.2296747>.
- Sun, W., G. Videen, S. Kato, B. Lin, C. Lukashin, and Y. Hu, 2011: A study of subvisual clouds and their radiation effect with a synergy of CERES, MODIS, CALIPSO, and AIRS data. *J. Geophys. Res.*, **116**, D22207, <https://doi.org/10.1029/2011JD016422>.
- Sun-Mack, S., P. Minnis, Y. Chen, S. Kato, Y. Yi, S. C. Gibson, P. W. Heck, and D. M. Winker, 2014: Regional apparent boundary layer lapse rates determined from CALIPSO and MODIS data for cloud-height determination. *J. Appl. Meteor. Climatol.*, **53**, 990–1011, <https://doi.org/10.1175/JAMC-D-13-081.1>.
- Trenberth, K. E., and J. M. Caron, 2001: Estimates of meridional atmosphere and ocean heat transports. *J. Climate*, **14**, 3433–3443, [https://doi.org/10.1175/1520-0442\(2001\)014<3433:EOMAAO>2.0.CO;2](https://doi.org/10.1175/1520-0442(2001)014<3433:EOMAAO>2.0.CO;2).
- , and J. T. Fasullo, 2008: An observational estimate of inferred ocean energy divergence. *J. Phys. Oceanogr.*, **38**, 984–999, <https://doi.org/10.1175/2007JPO3833.1>.
- , —, and M. A. Balmaseda, 2014: Earth's energy imbalance. *J. Climate*, **27**, 3129–3144, <https://doi.org/10.1175/JCLI-D-13-00294.1>.
- von Schuckmann, K., and Coauthors, 2016: An imperative to monitor Earth's energy balance. *Nat. Climate Change*, **6**, 138–144, <https://doi.org/10.1038/nclimate2876>.
- Wood, R., 2012: Stratocumulus clouds. *Mon. Wea. Rev.*, **140**, 2373–2423, <https://doi.org/10.1175/MWR-D-11-00121.1>.
- Wu, A., and Coauthors, 2013: Characterization of Terra and Aqua MODIS VIS, NIR, and SWIR spectral bands' calibration stability. *IEEE Trans. Geosci. Remote Sens.*, **51**, 4330–4338, <https://doi.org/10.1109/TGRS.2012.2226588>.
- Yang, K., R. T. Pinker, Y. Ma, T. Koike, M. M. Wonsick, S. J. Cox, Y. Zhang, and P. Stackhouse, 2008: Evaluation of satellite estimates of downward shortwave radiation over the Tibetan Plateau. *J. Geophys. Res.*, **113**, D17204, <https://doi.org/10.1029/2007JD009736>.
- Young, D. F., P. Minnis, D. R. Doelling, G. G. Gibson, and T. Wong, 1998: Temporal interpolation methods for the Clouds and the Earth's Radiant Energy System (CERES) experiment. *J. Appl. Meteor.*, **37**, 572–590, [https://doi.org/10.1175/1520-0450\(1998\)037<0572:TIMFTC>2.0.CO;2](https://doi.org/10.1175/1520-0450(1998)037<0572:TIMFTC>2.0.CO;2).